

The ALMA-ALPINE [CII] survey: The star formation history and the dust emission of star-forming galaxies at $4.5 < z < 6.2$

D. Burgarella¹, J. Bogdanoska¹, A. Nanni², S. Bardelli³, M. Béthermin¹, M. Boquien⁴, V. Buat^{1,32}, A. L. Faisst⁵, M. Dessauges-Zavadsky⁶, Y. Fudamoto^{7,8}, S. Fujimoto^{9,10}, M. Giavalisco¹¹, M. Ginolfi¹², C. Gruppioni¹³, N. P. Hathi¹⁴, E. Ibar¹⁵, G. C. Jones^{16,17}, A. M. Koekemoer¹⁴, K. Kohno^{18,19}, B. C. Lemaux^{20,21}, D. Narayanan²², P. Oesch^{6,9,10}, M. Ouchi^{18,23,24}, D. A. Riechers²⁵, F. Pozzi^{3,26}, M. Romano^{2,27,28}, D. Schaerer^{6,29}, M. Talia^{3,30}, P. Theulé¹, D. Vergani³, G. Zamorani³, E. Zucca³, P. Cassata³¹, and the ALPINE team

¹ Aix Marseille Univ, CNRS, CNES, LAM, Marseille, France
e-mail: denis.burgarella@lam.fr

² National Centre for Nuclear Research, ul.Pasteura 7, 02-093 Warszawa, Poland

³ INAF - Osservatorio di Astrofisica e Scienza dello Spazio di Bologna, via Gobetti 93/3 - 40129 Bologna - Italy

⁴ Centro de Astronomía (CITEVA), Universidad de Antofagasta, Avenida Angamos 601, Antofagasta, Chile

⁵ IPAC, California Institute of Technology, 1200 East California Boulevard, Pasadena, CA 91125, USA

⁶ Department of Astronomy, University of Geneva, ch. des Maillettes 51, CH-1290 Versoix, Switzerland

⁷ National Astronomical Observatory of Japan, 2-21-1, Osawa, Mitaka, Tokyo, Japan

⁸ Research Institute for Science and Engineering, Waseda University, 3-4-1 Okubo, Shinjuku, Tokyo 169-8555, Japan

⁹ Cosmic Dawn Center (DAWN), Jagtvej 128, DK2200, Copenhagen N, Denmark

¹⁰ Niels Bohr Institute, University of Copenhagen, Lyngbyvej 2, DK2100 Copenhagen, Denmark

¹¹ University of Massachusetts, 710 N. Pleasant St, LGRB-520, Amherst, MA 01003, USA

¹² European Southern Observatory, Karl-Schwarzschild-Str. 2, D-85748 Garching bei München, Germany

¹³ Istituto Nazionale di Astrofisica: Osservatorio di Astrofisica e Scienza dello Spazio di Bologna, Via Gobetti 93/3, 40129 Bologna, Italy

¹⁴ Space Telescope Science Institute, 3700 San Martin Drive, Baltimore, MD 21218, USA

¹⁵ Instituto de Física y Astronomía, Universidad de Valparaíso, Avda. Gran Bretaña 1111, Valparaíso, Chile

¹⁶ Cavendish Laboratory, University of Cambridge, 19 J. J. Thomson Ave., Cambridge CB3 0HE, UK

¹⁷ Kavli Institute for Cosmology, University of Cambridge, Madingley Road, Cambridge CB3 0HA, UK

¹⁸ Institute of Astronomy, School of Science, The University of Tokyo, 2-21-1 Osawa, Mitaka, Tokyo 181-0015, Japan

¹⁹ Research Center for the Early Universe, School of Science, The University of Tokyo, 7-3-1 Hongo, Bunkyo, Tokyo 113-0033, Japan

²⁰ Department of Physics, University of California, Davis, One Shields Ave., Davis, CA 95616, USA

²¹ Gemini Observatory, NSF's NOIRLab, 670 N. A'ohoku Place, Hilo, Hawai'i, 96720, USA

²² Department of Astronomy, University of Florida, 211 Bryant Space Sciences Center, Gainesville, FL 32611 USA

²³ Institute for Cosmic Ray Research, The University of Tokyo, 5-1-5 Kashiwanoha, Kashiwa, Chiba 277-8582, Japan

²⁴ Kavli Institute for the Physics and Mathematics of the Universe (WPI), The University of Tokyo, 5-1-5 Kashiwanoha, Kashiwa, Chiba 277-8583, Japan

²⁵ Cornell University, Space Sciences Building, Ithaca, NY 14853, USA

²⁶ Dipartimento di Fisica e Astronomia, Università degli Studi di Bologna, Via P. Gobetti 93/2, I-40129 Bologna, Italy

²⁷ Dipartimento di Fisica e Astronomia, Università di Padova, Vicolo dell'Osservatorio 3, I-35122, Padova, Italy

²⁸ INAF - Osservatorio Astronomico di Padova, Vicolo dell'Osservatorio 5, I-35122, Padova, Italy

²⁹ Institut de Recherche en Astrophysique et Planétologie - IRAP, CNRS, Université de Toulouse, UPS-OMP, 14, avenue E. Belin, F31400 Toulouse, France

³⁰ University of Bologna - Department of Physics and Astronomy "Augusto Righi" (DIFA), Via Gobetti 93/2, I-40129, Bologna, Italy

³¹ Dipartimento di Fisica e Astronomia Galileo Galilei Università degli Studi di Padova, Vicolo dell'Osservatorio 3, 35122 Padova Italy

³² Institut Universitaire de France, IUF, France

Received November XX, 2021; accepted ...

ABSTRACT

Star-forming galaxies are composed of various types of galaxies. However, the luminosity functions at $z \gtrsim 4 - 5$ suggest that most galaxies have a relatively low stellar mass ($\log M_{\text{star}} \sim 10$) and a low dust attenuation ($A_{FUV} \sim 1.0$). The physical properties of these objects are quite homogeneous. We used an approach where we combined their rest-frame far-infrared and submillimeter emissions and utilized the universe and the redshift as a spectrograph to increase the amount of information in a collective way. From a subsample of 27 ALMA-detected galaxies at $z > 4.5$, we built an infrared spectral energy distribution composite template. It was used to fit, with CIGALE, the 105 galaxies (detections and upper limits) in the sample from the far-ultraviolet to the far-infrared. The derived physical parameters provide information to decipher the nature of the dust cycle and of the stellar populations in these galaxies. The derived IR composite template is consistent with the galaxies in the studied sample. A delayed star formation history with $\tau_{\text{main}} = 500$ Myrs is slightly favored by the statistical analysis as compared to a delayed with a final burst or a continuous star formation history. The position of the sample in the star formation rate (SFR) versus M_{star} diagram is consistent with previous papers. The redshift evolution of the $\log M_{\text{star}}$ versus A_{FUV} relation is in agreement with an evolution in redshift of this relation. This evolution is necessary to explain the cosmic evolution of the average dust attenuation of galaxies. Evolution is also observed in the $L_{\text{dust}} / L_{FUV}$ (IRX) versus UV slope β_{FUV} diagram: younger galaxies have bluer β_{FUV} . We modeled the shift of galaxies in the IRX versus the β_{FUV} diagram with the mass-weighted age as a free parameter, and we provide an equation to make predictions. The large sample studied in this paper is generally consistent with models that assume rapid dust formation from supernovae and removal of dust by outflows and supernovae blasts. However, we find that high mass dusty star-forming galaxies cannot be explained by the models.

1. Introduction

Since the very first papers (e.g., Madau et al. 1996) on high redshift galaxies such as the Lyman break galaxies (LBGs), the issue of how much of their energy is emitted in the far-infrared (far-IR) has been an open question in the early universe. Today, a new question is coming to the forefront and we wonder what the dust cycle in high redshift galaxies is, that is how are large dust masses of dust formed at very high redshifts and efficiently destroyed or removed later, and what are the characteristics of these dust grains.

Thanks to deep observations with the Herschel space observatory (Herschel), the Atacama Large Millimeter/Submillimeter Array (ALMA) in the Southern Hemisphere, and the Northern Extended Millimeter Array (NOEMA) in the Northern Hemisphere, we have started to explore the dusty part of the spectral energy distributions (SEDs) of high redshift star-forming galaxies (Hiz-SFGs) (Bouwens et al. 2016; Burgarella et al. 2020; Sugahara et al. 2021; Hashimoto et al. 2019; Koprowski et al. 2020; Faisst et al. 2020; Faisst et al. 2020, and others) to obtain an overall view of the energy budget of normal star-forming galaxies in the early universe.

Still, except for lensed objects, targeted studies are not very successful and most of the Hiz-SFGs are not individually detected in the rest-frame far-IR, that is in the observed submillimeter (submm) and millimeter ranges (e.g., Bouwens et al. 2016; Bethermin et al. 2020; Burgarella et al. 2020; Faisst et al. 2020). Stacking remains the preferred tool to learn what the statistical dust properties of these galaxies are (e.g., Álvarez-Márquez et al. 2016, 2019; Carvajal et al. 2020).

Another interesting way to study these objects is through the far-IR fine-structure lines. These lines have been observed with the aim of understanding the interstellar medium properties and gas cooling in the neutral and ionized phases of local low-metallicity star-forming galaxies (e.g., Madden et al. 2013; Cormier et al. 2019; Fernández-Ontiveros et al. 2016). In the high redshift universe, several of these lines have also been identified (Harikane et al. 2014; De Breuck et al. 2019; Cunningham et al. 2020; Pavesi et al. 2019, for instance). We note that [OIII]88 μ m is very strong and may be the most intense line at high redshift where we expect that most galaxies contain a large population of O stars and have a low metallicity (Arata et al. 2020). Attempts at detecting [OIII]88 μ m have indeed been quite successful (e.g., Inoue et al. 2016; Hashimoto et al. 2019; Álvarez-Márquez et al. 2019). Since some of these lines (e.g., [OIII]88 μ m and [CII]158 μ m) are correlated with the star formation rate (SFR) of the galaxies, they can also be helpful when performing SED fitting by providing additional constraints on the recent SFR. Recently, the ALPINE-ALMA [CII] survey (Le Fèvre et al. 2020; Faisst et al. 2020; Bethermin et al. 2020) initiated an effort to detect the [CII]158 μ m line of 118 Hiz-SFGs in the redshift range $4.4 < z < 5.9$. The [CII]158 μ m line is one of the dominant gas coolants (Lagache et al. 2018). This line is detected in the ALPINE observations with an overall detection rate of 64% and a signal-to-noise ratio (S/N) threshold larger than 3.5σ . The ALPINE observations also allowed for the dust continuum of 23 of the 118 galaxies above 3.5σ to be detected (Bethermin et al. 2020).

The dust mass (M_{dust}) can be estimated from the observed flux density once we can assume a dust temperature (T_{dust}) and other dust-related physical parameters (e.g., Pozzi et al. 2021). However, even though it might seem obvious, estimating M_{dust} is much safer when using multiple data from the far-IR SEDs at different wavelengths. There is some degeneracy between T_{dust}

and M_{dust} , and more than a few data points lying both on the Rayleigh-Jeans (RJ) side, above the wavelength of the peak of the dust emission and on the Wien side, and below the peak wavelength of the dust emission which are important to constrain the SED (Liang et al. 2019). Because the individual approach is still quite a difficult task when dealing with the dust emission of galaxies close to or in the epoch of reionization (EoR), we need to combine the information from individual galaxies – assuming they share characteristic dust emission – to improve our wavelength coverage.

In this paper, we adopt a statistical approach using a sample of ALMA-observed high-redshift star-forming galaxies (ALPINE, Le Fèvre et al. 2020) the methodology already described in Burgarella et al. (2020) and Nanni et al. (2020). The redshifts of the final sample cover a range $4.5 \lesssim z \lesssim 6.2$ near or in the EoR that will be explored by the James Webb Space Telescope (JWST). The ALPINE sample is a unique source of data, which we combined to the one from Burgarella et al. (2020)¹ to build an IR composite template corresponding to the characteristic far-IR dust emission of Hiz-SFGs in the early universe. Some original works (e.g., Ouchi et al. 1999) have tried to use local starburst galaxies to build such templates and therefore estimate upper limits of submm flux densities. Similar to in Shapley et al. (2003) where a high S/N spectrum of $z \sim 3$ LBGs was derived, and even in a more similar way in Pearson et al. (2013) in which 40 H-ATLAS sources with previously measured redshifts in the range $0.5 < z < 4.2$ were used to derive a suitable average template for high-redshift H-ATLAS sources, the observed data from our sample were used to build the template.

In addition to using the composite IR SED to derive the dust properties of the galaxies via SED fitting, these data are also unique to help understand the stellar populations of these Hiz-SFGs and to calibrate important diagnostic diagrams in the early universe. Once an IR composite template is safely estimated from the observed ALMA detection, the spectral information in the rest-frame ultraviolet (UV), optical, and near IR is combined and we can come back to the individual approach to fit each galaxy.

In this paper, we assume a Chabrier initial mass function (IMF, Chabrier 2003). We use WMAP7 cosmology (Komatsu et al. 2011).

2. The sample of studied galaxies

The ALPINE sample is representative of the overall Hiz-SFGs population in the redshift range $4.5 \lesssim z \lesssim 5.5$. It is not dominated by IR-bright (i.e., in dust continuum) submm galaxies (SMGs). The ALPINE galaxies are mainly located on or near the main sequence (e.g., Rodighiero et al. 2011; Gruppioni et al. 2013; Donnari et al. 2019; Sherman et al. 2021) in the SFR versus stellar mass (M_{star}) relation observed at these redshifts (Speagle et al. 2014; Pearson et al. 2018). It is mostly dominated by UV-selected galaxies (see Table 1 in Faisst et al. 2020) with about 62% of the sample identified with the dropout technique, that is LBGs and 28% that are Lyman α emitters which were selected with narrow bands. We added, to the ALPINE galaxies, seven LBGs from Burgarella et al. (2020) and Nanni et al. (2020) to build our sample. The data of the latter seven LBGs were collected from several works (Bouwens et al. 2016; Capak et al. 2015; Faisst et al. 2017; Scoville et al. 2016; Willott et al. 2015;

¹ The combined ALPINE plus Burgarella et al. (2020) and Nanni et al. (2020) samples studied in this paper are referred to as our sample hereafter.

Hashimoto et al. 2018). This selection is certainly not complete and will very likely introduce biases on the results we obtained, but this is as good as we can currently do. The origins of the data are listed in Tab. 1.

Using Band-7 of ALMA, the ALPINE project observed a sample of galaxies with spectroscopic redshifts in two well-observed fields: 105 galaxies in the Cosmic Evolution Survey field (COSMOS, Scoville et al. 2007) and the remaining 13 in the Extended Chandra Deep Field South (ECDFS, Giacomini et al. 2002), with extensive multiband Hubble space telescope (HST) data from CANDELS (Grogin et al. 2011; Koekemoer et al. 2011). In this survey, 64% of the galaxies have been detected in [CII] at 3.5σ above the noise, as well as 21% of the galaxies detected in the continuum (S/N threshold corresponding to a 95% purity). The sample is divided into two redshift ranges at $4.40 < z < 4.65$ (median redshift $\langle z \rangle = 4.5$, containing 67 galaxies) and $5.05 < z < 5.90$ (median redshift $\langle z \rangle = 5.5$, containing 51 galaxies), separated by a gap in the transmission of the atmosphere. We note that type I active galactic nuclei (AGN), identified from broad spectral lines, are excluded from the present sample.

As the galaxies included in the ALPINE sample belong to well-studied fields, they come with a rich ancillary data set (Faisst et al. 2020). Due to the nature of the selection of these galaxies, they all have spectroscopic observations in rest-frame UV, performed with the Keck telescope and the European Very Large Telescope (VLT). A plethora of photometric observations are also available, from ground-based observatories in the UV to optical, from the Hubble space telescope (HST) in the UV, as well as from Spitzer above the Balmer break (all rest-frame features).

3. Methodology

The objective of the paper is to study the physical properties of the sample of Hiz-SFGs, and more specifically their stellar populations and dust grains. Because we do not have a wide wavelength coverage of their IR dust emission, we built an IR composite template from the subsample of ALMA-detected objects. To this aim, we applied the methodology described in Fig. 1 and it is detailed.

3.1. Building the IR composite template

3.1.1. Phase 0: Selection of the galaxies used to build the IR composite template

From the ALPINE sample and the one compiled by Burgarella et al. (2020), we selected the objects for which the dust continuum was detected with ALMA. More details on the selection are provided in Tab.1. The final sample of ALMA-detected objects contains 27 galaxies.

3.1.2. Phase 1: CIGALE initial individual fits of ALMA-detected galaxies to estimate the normalization at $\lambda = 200 \mu\text{m}$

The objective of this initial phase is to estimate a normalization factor for the SEDs of all the ALMA-detected galaxies. Galaxies with upper limits in the far-IR were not selected to build the IR composite SED. This normalization factor was derived from the estimated flux density at $\lambda = 200 \mu\text{m}$ (rest-frame), which is approximately the maximum wavelength above which we have no observed data. The SEDs of all the ALMA-detected objects

at $\lambda = 200 \mu\text{m}$ were set to 1.0 to build the IR composite SED. All the other data were modified accordingly. The spectral models selected in this initial fit are described in detail in Appendix A. We selected a wide range of models, especially for the dust emission which is important for this work.

We fit all the ALMA-detected galaxies using several options with CIGALE (see Appendix A for details on the priors for the models). CIGALE cannot model emission lines from photodissociation regions (PDRs). We used the [CII]158 μm fluxes to estimate the star formation rate ($\text{SFR}_{[\text{CII}]158\mu\text{m}}$), which we evaluated with the relation from Schaerer et al. (2020). These $\text{SFR}_{[\text{CII}]158\mu\text{m}}$ values, along with the associated uncertainties derived from the line uncertainties, were added as properties to constrain the CIGALE SED fitting². To perform this analysis, we selected three types of dust emission available in CIGALE: i) a mid-IR power law and a general modified blackbody (Casey 2012): PL+G_MBB, ii) a mid-IR power law and an optically thin modified blackbody (Casey 2012): PL+OT_MBB, and, iii) the models from Draine et al. (2014): DL2014.

It is specifically worth checking whether the prior assumptions made on the emissivity index (β_{RJ}) of the modified blackbody could bias the final result. We could not safely estimate β_{RJ} for the individual objects but we could do so better with the IR composite template because more data points are used, thus we also fixed $\beta_{RJ} = 1.0, 1.5,$ and 2.0 to test the impact on the level of the luminosity at $200 \mu\text{m}$ (rest-frame) used for the normalization of the individual SEDs. Table 2 shows that the bias introduced by the initial prior on β_{RJ} is much lower than the uncertainties comings from the values derived by an SED fitting. However, we would like to stress that a wide range of SED shapes were used to estimate the normalization, including several β_{RJ} , T_{dust} , and DL2014 models.

3.1.3. Phase 2: Building of the IR composite template

In this second phase, we proceeded by actually building the observed composite IR template. For this, we made use of the normalized SEDs of each of the 27 ALMA-detected objects.

- **Phase 2.1: Checking the homogeneity in the galaxy sample \rightarrow IRV1 template:** By making use of the normalization factors and benefiting from the redshift coverage ($4.3 < z < 6.2$), we used the universe as a spectrograph and we combined the SEDs of 27 ALMA-detected objects to form an initial version (IRV1) of the observed composite SED (Fig. 1, Fig. 2). We note that this process is different from the stacking method whose aim is to detect the average flux density at a given wavelength of a sample of detected and/or undetected objects.

We began by verifying whether the subsample of ALMA-detected galaxies is homogeneous enough to build a single IR composite template. For instance, one single object or all the objects in a given redshift range might significantly impact the parameters of the dust emission and bias the IR composite template. Here, we only show the results of this test assuming PL+OT_MBB, but we checked that the results were the same regardless of the assumed dust emission option.

² By comparing the results of the fits with and without [CII]158 μm , we get the following: $M_{star}([\text{w}/\text{CII}]) / M_{star}([\text{w}/\text{CII}]) = 0.90 \pm 0.27$, $\text{SFR}([\text{w}/\text{CII}]) / \text{SFR}([\text{w}/\text{CII}]) = 1.22 \pm 0.32$, $L_{dust}([\text{w}/\text{CII}]) / L_{dust}([\text{w}/\text{CII}]) = 1.22 \pm 0.27$, and $L_{FUV}([\text{w}/\text{CII}]) / L_{FUV}([\text{w}/\text{CII}]) = 1.02 \pm 0.02$ with no significant difference for the selected dust emission type.

Source	Number of objects	Selection	redshift	Notes
Le Fèvre et al. (2020); Faisst et al. (2020); Bethermin et al. (2020)	118	SFG	$z \sim 4.5$ $z \sim 5.5$	* 20 ALMA-7 detections with $S/N > 3$ * 78 ALMA-7 upper limits * 18 ALMA-7 not selected (not enough data) * $S/N_{UV-optical-NIR} > 2.5$. * SFG with > 5 data points in UV-optical only * [CII]158 μm measurements for 64% of the sample
Capak et al. (2015) & Faisst et al. (2017)	4 (HZ4, HZ6, HZ9, HZ10)	UV	$z \sim 5.6$	* [CII]158 μm for all Hi-z LBGs * ALMA-7 detections: HZ4, HZ6 (3) HZ9 & HZ10 (5) * ALMA-7 upper limits for the others * HZ5 detected in Chandra and not included in the sample * Additional data from Pavesi et al. (2016)
Scoville et al. (2016)	1 (566428)	UV	$z = 5.89$	* ALMA-6 detection * [CII]158 μm measurement
Willott et al. (2015)	2 (CLM1 & WMH5)	UV	$z \sim 6.1$	* ALMA-6 detections * [CII]158 μm measurement

Table 1: Origins of the data used in this paper. The final sample used in this paper contains 105 objects: 27 with ALMA detections and 78 with ALMA upper limits. The other objects were discarded from the sample because they do not have enough data in the UV-optical-near-IR range to perform a safe SED fitting.

β_{RJ}	$\Delta L_{200\mu\text{m}} = \frac{\langle L_{200\mu\text{m}} \rangle - L_{200\mu\text{m}}^{\beta_{RJ}}}{\langle L_{200\mu\text{m}} \rangle}$	$\sigma(\Delta L_{200\mu\text{m}})$	$[\Delta L_{200\mu\text{m}}]_{\text{err}}$ from SED fitting
1.0	-0.022	0.118	0.501
1.5	-0.013	0.049	0.466
2.0	0.035	0.060	0.825

Table 2: Parameters of the dust emission. The results shows that whatever the prior on the value of β_{RJ} , the dispersion on the resulting normalization factor is negligible and much smaller than the uncertainties on the luminosity at $|\lambda = 200\mu\text{m}$ (rest frame) derived from the SED fitting and used for the normalization of the individual SEDs. This means that the method adopted to estimate the normalization factor does not significantly impact the shape of the final IR composite template.

To reach this goal, we used the knife-jacking method, where we removed the SED of each galaxy (or a series of galaxies in a redshift range) sequentially from the list of objects, built the composite template, and fit it with CIGALE. Then, we put the removed objects back in the detected subsample and we reproduced this operation recursively as many times as there were objects (or series of galaxies in a redshift range) in the subsample. At the end, we could compare the parameters from the several composite templates built from $N_{obj} - N_{removed-obj}$ and we checked whether they were consistent.

From the analysis on individual objects (Fig. 3), we discovered that only when removing HZ10 at $z=5.659$ did we get slightly different values for T_{dust} and β_{RJ} . However, it does not significantly bias the parameters defining the shape of the composite template. We decided to keep it in the sample because it contributes to the representativity of the studied

galaxies. The dust parameters are very stable with average values at $T_{dust} \approx 54\text{K}$ and $\beta_{RJ} \approx 0.9$.

From the analysis on redshift ranges, we discovered that the redshift range $5.0 < z < 6.0$ brings the objects with the widest wavelength range to the IR composite SED. Without the ALMA-detected galaxies in the range $5.0 < z < 6.0$, there was a difference for T_{dust} and β_{RJ} (Tab. 3). But again, the results are in agreement within the uncertainties, even though an evolution within the uncertainties cannot be ruled out.

This second phase provided an IR composite template IRV1 shown as green points in Fig. 2.

removed z range	$N_{removed-obj}$	β_{RJ}	T_{dust}
$4.0 < z < 5.0$	62	0.84 ± 0.28	54.3 ± 6.7
$5.0 < z < 6.0$	41	1.30 ± 0.55	47.6 ± 8.4
$6.0 < z < 7.0$	2	0.85 ± 0.28	53.7 ± 6.6

Table 3: Degeneracy of β_{RJ} and T_{dust} . Results of the knife jacking method applied on the entire sample when removing and adding back objects in the given redshift ranges from the first column to build the composite template. The dust parameters are stable. Even though it is still consistent with the other ones, the results without one redshift range (namely $5.0 < z < 6.0$) differ. This could be explained because the $5.0 < z < 6.0$ range contains the widest wavelength range and it is therefore more constraining to estimate β_{RJ} and T_{dust} . So, we cannot rule out a small variation of these two parameters with the redshift inside the quoted uncertainties.

- **Phase 2.2: Checking if the stacked data from Bethermin et al. (2020) are in agreement with the IRV1 \rightarrow IRV2 template:** In addition to the main ALPINE data, Bethermin et al. (2020) stacked data from two galaxy samples at $z \sim 4.5$ and $z \sim 5.5$ with Herschel (Pilbratt et al. 2010) data from the PEP (Lutz et al. 2011) and HerMES (Oliver et al. 2012) surveys

and AzTEC/ASTE data from Aretxaga et al. (2011) at 1.1 mm. At 850 μm , they used the SCUBA2 data from Casey et al. (2013). This data set can be very useful because it extends the wavelength range to the mid-IR. However, because there are not enough ALPINE sources to obtain a sufficiently high S/N in the stacked Herschel data, the ALPINE selection was not used for the stacking. Bethermin et al. (2020) define two redshift bins ($4 < z < 5$ and $5 < z < 6$) that match the redshift ranges probed by ALPINE. Before further continuing to fulfill our task of building the LBG composite IR template, we first need to assess whether the $z \sim 4.5$ and/or $z \sim 5.5$ stacks are consistent with the IRV1 composite IR template. Our analysis allows us to conclude that both stacks are consistent (all χ^2_ν from the SED fitting have $\sim 0.3 - 0.4$) with the ALMA-detected galaxies' composite IR template built by combining the full sample of the 27 ALMA-detected objects. The final IR composite template (IRV2, Fig. 2) was built from the ALMA-detected galaxies from Burgarella et al. (2020), the ALPINE sample, in addition to the two stacks from Bethermin et al. (2020).

In Tab. ??, we provide the IR composite template based on the observed data and show the fits with the three dust emissions from 1 μm to 1000 μm fitted in Fig. 4. The modeled SEDs from 20 μm to 1 mm are listed in Tab. D.1.

3.1.4. Fitting the IR composite template

The main dust parameters derived from fitting the observed IRV2 IR composite template (Fig. 4) are listed in Tab. 4. The objects in the present sample are Hiz-SFGs with a low dust attenuation (e.g., Faisst et al. 2020, and later in this paper). This assumption is valid for the ALPINE sample (Faisst et al. 2020). Therefore, we make the assumption that the best emission models for these objects should be optically thin. We checked this hypothesis by estimating the following (Eq. 2 in Jones et al. 2020):

$$\tau_\nu = \frac{M_{dust}}{A_{gal}} \kappa_\nu$$

where τ_ν is the optical depth, M_{dust} is the dust mass, A_{gal} is the area covered by the galaxy, and κ_ν is the dust mass absorption coefficient:

$$\kappa_\nu = \kappa_0 (\nu / \nu_0)^{\beta_{RJ}}$$

where ν_0 is the frequency where the optical depth equals unity and β_{RJ} is the spectral emissivity index from the Rayleigh-Jeans range. We tested the opacity both with the optically thin and with the general modified black bodies (Casey 2012). The median radius of the galaxies are $r_{e,[CII]} = 2.1 \pm 0.16$ kpc (Fujimoto et al. 2020) to estimate A_{gal} . Both provide values that are in the range $[10^{-4} - 10^{-2}]$, that is $\tau_\nu \ll 1.0$, which confirms that the optically thin assumption is valid here. In the rest of the paper, we only make use of DL2014 and PL+OT_MBB dust emissions.

After fitting the IR composite template, we derived values for T_{dust} and β_{RJ} (Tab. 4). However, these dust parameters are known to be degenerate depending on the S/N and the wavelength sampling of the far-IR SED (e.g., Juvela et al. 2013; Tabatabaei et al. 2014). This degeneracy is a serious problem when using only one or a few data points in the far-IR. However, using the derived IR composite template helps to remove the degeneracy. We tested how well T_{dust} and β_{RJ} can be estimated by performing fits with fixed T_{dust} and varying β_{RJ} , then by fixing β_{RJ} and keeping T_{dust} free. The results are compared to the parameters derived by keeping both parameters free in Fig. 5. Even though we can see

the usual regular evolution of T_{dust} with β_{RJ} (or vice versa), the quality of the fit with fixed parameters improves when getting closer to the Bayesian values derived with CIGALE when both parameters are free (Tab. 4).

	PL+G_MBB	PL+OT_MBB	DL2014
α_{MIR}	2.23 \pm 0.63	2.00 \pm 0.82	N/A
β_{RJ}	1.43 \pm 0.47	0.87 \pm 0.28	N/A
T_{dust} [K]	65.5 \pm 5.1	54.1 \pm 6.7	N/A
q_{PAH}	N/A	N/A	0.47
α	N/A	N/A	2.39 \pm 0.44
u_{min}	N/A	N/A	18.1 \pm 12.7
γ	N/A	N/A	0.54 \pm 0.35
$L_{dust}/10^{20}$ [W]	2.84 \pm 0.14	2.43 \pm 0.12	2.57 \pm 0.13

Table 4: Main relevant physical parameters derived by fitting the IR template with the various assumptions of the dust emission: PL+G_MBB is based on a power law in the mid-IR plus the general blackbody formula as in Casey et al. (2012); PL+OT_MBB is a power law in the mid-IR (α_{MIR}) plus an optically thin blackbody, which is again similar to Casey et al. (2012); and DL2014 stands for Draine & Li (2014) models. The parameters are described in Appendix A. Because the SEDs were normalized to 1.0 at $\lambda = 200\mu\text{m}$, the values of L_{dust} can be directly compared.

The value of $\beta_{RJ} = 0.87 \pm 0.28$ for a power law plus optically thin modified blackbody found in this paper is low, but comparable to the minimum values found by Bendo et al. (2003); Galametz et al. (2012), for example, for nearby galaxies in the range $0.8 < \beta_{RJ} < 2.5$. Lower β_{RJ} closer to 1.0 were estimated when fitting different types of galaxies and more specifically very low-metallicity galaxies such as SBS 0335-052 (Hunt et al. 2014), NGC 1705 (O'Halloran et al. 2010), and even low-metallicity regions in very nearby galaxies with excellent coverage to estimate β_{RJ} similar to Messier 33, for instance (Tibbs et al. 2018; Tabatabaei et al. 2014). Tabatabaei et al. (2014) found an apparent decrease in both T_{dust} and β_{RJ} with an increasing M33 radius. This corresponds to regions with low metallicities and they propose that the effect could help to find an origin in the different grain compositions and, possibly, different size distributions. Assuming such β_{RJ} values for Hiz-SFGs would mean that the mean dust temperature could be higher than T_{dust} estimated with emissivities in the range $1.5 < \beta_{RJ} < 2.0$. This result ($\beta_{RJ} \sim 1$) needs to be further confirmed for the SEDs of similar low- M_{star} , low- A_{FUV} galaxies with a better RJ wavelength coverage.

The value of T_{dust} found from the IR composite template ($54.1 \pm 6.7\text{K}$) should be compared to other ALMA-based dust temperatures for objects at high redshift ($z > 4.5$). In a recent paper, Bakx et al. (2021) present the evolution of T_{dust} for "normal" (i.e., main sequence) galaxies from $z \sim 0$ to $z \sim 8$. A linear increase is suggested up to $z = 6$. At larger redshifts, a large dispersion in T_{dust} can be noticed even though the linear relation might hold, given the large uncertainties (Faisst et al. 2020; Harikane et al. 2020; Sugahara et al. 2021; Laporte et al. 2019). Bakx et al. (2021) show that adding ALMA Band 9 significantly reduces the uncertainty on the dust temperature for a single object by further constraining the shape of the SED. At the mean redshift $z = 4.94 \pm 0.54$ of our entire sample, the dust temperature that could be estimated assuming the linear relation from Fig. 4 in Bakx et al. (2021) would be $T_{dust} \approx 49\text{K}$, which is not significantly different

from our estimation of $54.1 \pm 6.7\text{K}$. However, Bakx et al. (2021) derived a value of $\beta_{RJ} = 1.61 \pm 0.60$ which is larger than the one found in the previous paragraph. Both are consistent if we account for the uncertainties. Lower values for β_{RJ} mean higher dust temperatures, as shown in Fig. 5. Thus measuring β_{RJ} with a good sampling of the RJ part of the spectrum is important to address the question about the decrease in β_{RJ} in low-metallicity regions toward the outskirts of local galaxies and in some local low-metallicity galaxies. If so, the increase in dust temperature might be larger than when evaluated with $\beta_{RJ} \sim 1.5 - 2.0$.

3.2. Phase 3: Far-UV to far-IR fit of individual galaxies with the IR composite template

We now fit the complete sample of objects assuming the dust emission from the IRV2 composite SED. The rest-frame UV, optical, and near IR ranges are useful when constraining the stellar emission and, therefore, the properties of the stellar populations. However, attenuation also impacts the rest-frame UV spectral range, which is therefore useful to constrain the amount of dust attenuation. The assumptions used when fitting the entire galaxy sample with CIGALE are given in Tab. B.1. We focus on the properties of the stellar populations and the dust attenuation in these objects.

Even though the Bayes factor is conceptually more conclusive, its computation can still be very complex. We need to compute a quantity called the marginal likelihood or evidence ($P(D/M_i)$), where D are the photometric data and M_i are each model, which implies computing a very complicated and time-consuming integral because the likelihood of observation D under the model M_i must quantify over all possible parameters of that model. An analytic computation is almost never possible and direct evaluation by numerical quadrature is almost never feasible for models of real-world dimensionality and complexity. This is why a variety of approximations based on special properties of the models or their posterior distributions were developed Kass & Raftery (1995).

Generally, it is found that the conclusions drawn from the Bayes factor are more satisfying, but also more complex methodologies have not been qualitatively very different from those drawn from the simpler BIC method (Raftery 1998). However, we can elaborate on the use of the BIC versus Bayes Factor for our specific case. From Raftery (1998), we determined that in our case, the unit information prior should reasonably cover the range of observed data because we have a homogeneous sample of galaxies and we have a rough idea of the general range within which the data are likely to lie in advance. So we defined our priors to homogeneously cover the expected range of parameters. Volinsky (1997) showed, via simulations, that the performance of Bayes factors can be better than that of BIC if the prior used is spread out less than the unit information prior. In our case, the unit information prior is quite spread out (see Table 5) and BIC should be at least as good as the Bayes factor. Because of this spread out prior, BIC provides more conservative results. Also, if an effect is favored by BIC, this should be a solid result. On the other hand, if BIC does not favor an effect, it might still be possible that another, justifiable prior could change the conclusion. For us, that means that the most conclusive results would be that an SFH that includes a burst is solidly ruled out when compared to a delayed SFH with $\tau = 500$ Myrs SFH.

We decided to use the Bayesian information criterion (BIC) test to compare the various hypotheses made on the dust emission and on the star formation history in Fig. 6. To interpret the

results from the BIC tests, we refer to Kass & Raftery (1995):

$$BIC = \chi^2 + k \ln(n)$$

where k is the number of model parameters in the test and n is the sample size, that is to say the number of pieces of photometric data in our case. When comparing several models, the one with the lowest BIC is preferred. To interpret the results, $0 < \Delta BIC < 2$ means that evidence for a difference between the two hypotheses is faint ($2 < \Delta BIC < 6$ means positive, $6 < \Delta BIC < 10$ means strong, and $\Delta BIC > 10$ means very strong).

We start by comparing the two dust emission models, DL2014 (Draine et al. 2014) and PL+OT_MBB (Casey 2012), available in CIGALE. Tab. 5 presents all the results of the BIC analysis on our sample of Hiz-SFGs, numerically. The histogram of ΔBIC values strongly peaks at 0 with a small tail extending to $\Delta BIC = -4$ (Fig. 6), meaning that we do not see any strong difference between DL2014 and PL+OT_MBB when fitting our sample. However, for a minority of objects, PL+OT_MBB might be favored. We show the results using both DL2014 and PL+OT_MBB later in the paper. However, in general, no significant difference as to the quality of the fit is observed, confirming the BIC analysis.

We now focus on the comparison between the various SFHs. Fig. 6 shows the results of the BIC analysis by comparing the various kinds of SFHs used in the CIGALE analysis. We note that we only used the initial observed data and not the IR composite template. The only significant difference is that a simple delayed SFH with $\tau_{main} = 500$ Myrs without any final burst is preferred to a delayed SFH with a burst. A constant SFH (with $\tau_{main} = 20$ Gyrs) and multi- τ_{main} are weakly disfavored when compared to a simple delayed SFH with $\tau_{main} = 500$ Myrs. These comparisons are compatible with both DL2014 and PL+OT_MBB. There is some dispersion in the results which suggests that the preferred modeling for the entire galaxy population might not be valid for each individual galaxy, as shown in Fig. 6.

In order to move a little bit further with our comparison of the models, we performed a mock analysis with CIGALE from the initial fit, again without using the IR composite template. We selected the PL+OT_MBB and DL2014 options for the dust emission in Fig. C.1. In brief, for each object, the CIGALE mock analysis consists in using the best fit model for each object to generate an input photometric catalog (called a mock catalog) to which we randomly added uncertainties drawn inside a Gaussian distribution with σ corresponding to the observed uncertainties (see Boquien et al. 2019). The SED fitting procedure was applied in the very same way as when fitting the observed SEDs. Then, we compared the derived output parameters to those of the known input (Fig. C.1). The results from this mock analysis (Tab. 6) show that both for the PL+OT_MBB and for the DL2014 dust emissions, we were able to recover the main physical parameters related to the SFH and to the dust emission. This means that we do not expect strong degeneracies ($r^2 = 0.80$ shown in Fig. C.1, where r is Pearson's correlation coefficient commonly used in linear regression). The mean value and standard dispersion of the main parameters derived from the individual fits of our galaxy sample are given in Tab. 7 and the individual values for the same parameters are listed in Tab. E.2 and Tab. E.2 in Appendix E (available online) in their entirety.

DL2014 vs. PL+OT_MBB									
τ_{main} [Myr]	k	Age _{main} [Myrs]	τ_{burst} [Myr]	Age _{burst} [Myrs]	δ	Mean	SD	Min	Max
500 Myrs	2 ≤ k ≤ 5	101 values in [2, 1200]				-0.95	1.58	-7.28	4.08
DL2014									
τ_{main} [Myr]	k	Age _{main} [Myrs]	τ_{burst} [Myr]	Age _{burst} [Myrs]	δ	Mean	SD	Min	Max
20000 Myrs	2 ≤ k ≤ 5	101 values in [2, 1200]				-3.35	11.21	-68.37	1.39
10 values in [100, 1000]	3 ≤ k ≤ 6	101 values in [2, 1200]				-0.75	5.83	-3.15	41.64
500	3 ≤ k ≤ 6	101 values in [100, 1200]	20000	2, 5, 10, 20, 50		-1.62	5.87	-9.23	16.89
500	3 ≤ k ≤ 6	101 values in [2, 1200]				1.49	7.12	-3.59	43.43
								7 values in [-0.70, 0.70]	
PL+OT_MBB									
τ_{main} [Myr]	k	Age _{main} [Myrs]	τ_{burst} [Myr]	Age _{burst} [Myrs]	δ	Mean	SD	Min	Max
20000 Myrs	2 ≤ k ≤ 5	101 values in [2, 1200]				-3.49	11.40	-68.37	1.55
10 values in [100, 1000]	3 ≤ k ≤ 6	101 values in [2, 1200]				-0.67	6.00	-3.15	41.64
500	3 ≤ k ≤ 6	101 values in [100, 1200]	20000	2, 5, 10, 20, 50		-1.05	6.57	-9.23	19.16
500	3 ≤ k ≤ 6	101 values in [2, 1200]				1.51	7.20	-3.04	42.94
								7 values in [-0.70, 0.70]	

Table 5: Comparison of the reference model (SFH delayed: $t/\tau^2 \exp(-t/\tau)$ with $\tau = 500$ Myrs) to all the others using the BIC. This comparison was performed by fitting all the objects in our sample. We note that the IR composite SED is not used in this analysis, but only individual ALMA measurements (detections and upper limits). We first assumed a DL2014 model for the IR template. The, we assumed a PL+OT_MBB for the IR template. The BIC values do not change much for the two options for the IR template. The range in the number of parameters k is also indicated for each series of run. To the parameters listed in the table, we need to add the amount of dust attenuation, i.e., $E_{-BV_s_young}$. The sample has at least five photometric points in the rest-frame UV and optical as well as one photometric point in the rest-frame far-IR, so $n \geq 7$. More precisely, the complete sample of individual galaxies have $7 \leq n \leq 24$ with $\langle n \rangle = 13.3 \pm 4.3$ and 11/119 objects have more than ten photometric points.

Run	L_{dust}	L_{FUV}	IRX	M_{dust}	$\beta_{cal:94}$	SFR _{10Myrs}	t_{burst}	age _{burst}	τ_{main}	age _{main}	δ	M_{star}	A_{FUV}
$\tau_{500Myrs_dl2014}$	0.98	0.89	0.91	0.98	0.89	0.96				0.81		0.95	0.92
$\tau_{500Myrs_casey2012_OT}$	0.98	0.84	0.87	0.98	0.84	0.96				0.80		0.93	0.85
$\tau_{20000Myrs_dl2014}$	0.97	0.92	0.89	0.97	0.87	0.95				0.71		0.94	0.89
$\tau_{20000Myrs_casey2012_OT}$	0.98	0.90	0.89	0.98	0.87	0.97				0.74		0.95	0.89
$\tau_{500Myrs_dl2014_burst}$	0.96	0.90	0.88	0.96	0.91	0.93	0.47	0.05		0.46		0.96	0.93
$\tau_{500Myrs_casey2012_OT_burst}$	0.96	0.94	0.90	0.96	0.89	0.91	0.27	0.06		0.42		0.94	0.92
τ_{multi_dl2014}	0.98	0.56	0.87	0.98	0.73	0.96			0.20	0.65		0.13	0.90
$\tau_{multi_casey2012_OT}$	0.98	0.64	0.88	0.98	0.80	0.97			0.18	0.62		0.19	0.91
$\tau_{500Myrs_dl2014_delta}$	0.99	0.93	0.90	0.99	0.85	0.97				0.78	0.37	0.94	0.89
$\tau_{500Myrs_casey2012_OT_delta}$	0.98	0.92	0.79	0.98	0.56	0.97				0.79	0.35	0.92	0.62

Table 6: Summary of the power of two for correlation coefficients, r^2 , from the mock analysis on the main physical parameters performed by CIGALE. The delayed SFH with $\tau_{main} = 500$ Myrs is shown with "tau500" in the legend. If a final burst was added, "burst" is used in the legend. A constant SFH with $\tau_{main} = 20$ Gyrs is shown with "tau20000" in the legend, and multi- τ_{main} is shown as "multitau" in the legend.

Parameter	DL2014	PL + OT_MBB
$M_{star} [M_{\odot}]$	$(1.18 \pm 0.19) \times 10^{10}$	$(1.18 \pm 0.18) \times 10^{10}$
$SFR [M_{\odot} yr^{-1}]$	47.6 ± 5.1	46.8 ± 5.0
$M_{dust} [M_{\odot}]^*$	$(5.64 \pm 0.69) \times 10^7$	$(2.07 \pm 0.25) \times 10^7$
$L_{dust} [L_{\odot}]$	$(3.38 \pm 0.41) \times 10^{11}$	$(3.32 \pm 0.40) \times 10^{11}$
$L_{FUV} [L_{\odot}]$	$(1.07 \pm 0.06) \times 10^{11}$	$(1.06 \pm 0.06) \times 10^{11}$
$sSFR [yr^{-1}]$	$(1.16 \pm 0.34) \times 10^{-8}$	$(1.15 \pm 0.34) \times 10^{-8}$
sM_{dust}^*	0.010 ± 0.003	0.004 ± 0.001
IRX	0.31 ± 0.14	0.31 ± 0.13
A_{FUV}	1.14 ± 0.15	1.14 ± 0.15
age _{main} [Myr]	440 ± 98	444 ± 98

Table 7: Mean value and standard deviations of the physical parameters derived from the fit analysis of the individual objects in our sample. The Bayesian outputs are listed here. *The values listed in the table are those computed with $\kappa_0 = 0.637 \text{ m}^2 \text{ kg}^{-1}$, corresponding to Draine et al. (2014). For $\kappa_0 = 0.45 \text{ m}^2 \text{ kg}^{-1}$ [$\kappa_0 = 0.72 \text{ m}^2 \text{ kg}^{-1}$, respectively], that is before [after, respectively] the reverse shock, we found the following: $M_{dust} = (2.91 \pm 0.35) \times 10^7 M_{\odot}$ [$M_{dust} = (1.82 \pm 0.22) \times 10^7 M_{\odot}$, respectively] and $sM_{dust} = 0.005 \pm 0.002$ [$sM_{dust} = 0.003 \pm 0.001$, respectively].

4. Analysis of the results

From the previous analysis, we derived a set of physical parameters for each of the galaxies in our sample. These parameters allowed us to define and build diagnostic diagrams that permitted us to characterize these galaxies and, more specifically, their SFH and their dust properties. We analyzed the locations of our sample in the IRX versus β_{UV} diagram, the A_{FUV} versus M_{star} diagram, and in the specific dust mass versus specific star forma-

tion rate: sM_{dust} versus $sSFR = M_{dust} / M_{star}$ versus SFR / M_{star} (dust formation rate diagram or DFRD).

4.1. The SFR versus M_{star} diagram

Fig. 7 presents the SFR versus M_{star} diagram³. The points corresponding to this work are found in the expected range when

³ We only present the results using the reference SFH derived in the present section, i.e., delayed SFH(t) = $t/\tau_{main}^2 \exp(t/\tau)$ with $\tau_{main} =$

compared to Pearson et al. (2018) who also used CIGALE:

$$\log_{10}(SFR) = (1.00 \pm 0.22) (\log_{10}(M_{star}) - 10.6) + (1.92 \pm 0.21)$$

and compared to Speagle et al. (2014) with their "mixed" (preferred fit)":

$$\log_{10}(SFR) = [(0.73 \pm 0.02) - (0.027 \pm 0.006) \times t[\text{Gyr}]] \log_{10}(M_{star}) - [(5.42 \pm 0.22) + (0.42 \pm 0.07) \times t[\text{Gyr}]]$$

function evaluated at $z = 5.0$ (i.e., $t_{universe} = 1.186$ Gyr), which was converted to a Chabrier IMF by subtracting 0.03 to $\log_{10}(SFR)$ and to $\log_{10}(M_{star})$. The first result is that regardless of the dust emission used (DL2014 or PL+OT_MBB), we found about the same main sequence. Our data are in good agreement with Faisst et al. (2020) and Khusanova et al. (2021) and also they generally follow the relations derived by Speagle et al. (2014) and Pearson et al. (2018). Most of the detections are found at a relatively large stellar mass ($\log_{10}(M_{star}) \sim 10$). We confirm the evolution of the main sequence to $z = 4.5 - 5.5$ with our sample of galaxies (mainly objects not detected in dust continuum), which extend to $\log_{10}(M_{star}) \sim 8.5$.

4.2. The A_{FUV} versus M_{star} diagram

The relation between the dust attenuation (A_{FUV} or its proxy, $IRX = L_{dust} / L_{FUV}$) and the stellar mass (M_{star}) is another way to estimate the dust attenuation in galaxies without far-IR data. This relation between the stellar mass and dust attenuation has been the focus of numerous studies (as early as Xu et al. 2007; Buat et al. 2009, and references therein). However, even if this relation could be very useful in addition to the IRX versus β_{FUV} one ($f_{\lambda} \propto \lambda^{\beta_{FUV}}$), the link between the far-UV (FUV) dust attenuation and the stellar mass (A_{FUV} versus M_{star}) is not well established at all redshifts.

Bouwens et al. (2016) define what a consensus relation could be: $\log_{10}(IRX) = \log_{10}(M_{star}/M_{\odot}) - 9.17$ assuming the dust temperature evolves with the redshift. This relation is linear in the plane $\log_{10}(IRX)$ versus $\log_{10}(M_{star}/M_{\odot})$, and in the range $9.0 < \log_{10}(M_{star}/M_{\odot}) < 11.0$. In a recent paper, Carvajal et al. (2020) used the stacking method for 1582 UV LBGs with photometric redshifts in the range $z \sim 2 - 8$ to reach down to $\log_{10}(M_{star}/M_{\odot}) = 6.0$. However, the constraints from this stacking are only upper limits, which are less useful than detections (see their Fig. 16). Fudamoto et al. (2020) made use of the ALPINE data and show that the $\log_{10}(IRX)$ versus M_{star} relation derived from their observations is inconsistent with the previously determined relations at $z \leq 4$. They found a fast decrease in IRX at $z \sim 4$ in massive galaxies which suggests an evolution of the average amount of dust attenuation in star forming galaxies. Bernhard et al. (2014) assume an evolving normalization of the $\log_{10}(IRX)$ versus $\log_{10}(M_{star})$ relation in the low redshift universe at $z < 1$. We need an opposite evolution (lower in IRX) in the high redshift universe at $z > 4$ as in Bogdanoska & Burgarella (2020).

Fig. 8 shows that the two M_{star} stacks from Fudamoto et al. (2020) at $z \sim 4.5$ are marginally (accounting for the uncertainties) in agreement with Bogdanoska & Burgarella (2020). They are in better agreement at $z \sim 5.5$. However, the low stellar mass range is crucial, especially in the early universe where galaxies are expected to have lower stellar masses because they were still building their stars at that time. From our analysis, we confirm the effect found by Fudamoto et al. (2020): our galaxies have

500Myrs, but with the following two options for dust emission: Draine et al. (2014) and a power law in a mid-IR and optically thin blackbody.

lower A_{FUV} or IRX values at a fixed mass, compared to previously studied $IRX-M_{star}$ relations at $z < 4$, with quite a large scatter.

In order to constrain the amount of dust attenuation of these low-mass galaxies, it is possible to adopt a global approach and compare what the hypothesis on the A_{FUV} versus $\log_{10}(M_{star})$ implies for the redshift evolution of the average dust attenuation in the universe as presented in Cucciati et al. (2012); Burgarella et al. (2013); Madau & Dickinson (2014), for example. Using this approach, Bogdanoska & Burgarella (2020) conclude that it is not possible to extend a linear relation to the lowest mass range without strongly underpredicting the average dust attenuation in the universe at all redshifts. We need a flattening of the relation at low stellar mass ($\log_{10}(M_{star}/M_{\odot}) < 9.0$). This means that the apparent dust attenuation of the low-mass galaxies is significantly higher than 0. This very interesting and unexplained point is also suggested by other observational and theoretical works (e.g., Salim et al. 2016; Takeuchi et al. 2010; Cousin et al. 2019; Ma et al. 2016). They propose modeling the A_{FUV} versus M_{star} relation with the following broken law:

$$A_{FUV} = \begin{cases} a \times 1.1 & \text{at } \log_{10}M_{star} < 9.8 \\ a \times (\log_{10}M_{star} - 8.7) & \text{at } \log_{10}M_{star} \geq 9.8 \end{cases} \quad (1)$$

where $a = (z + \gamma) \times \alpha^{\beta - (z + \gamma)}$ with z being the redshift and the constants $\alpha = 1.84 \pm 0.11$, $\beta = 1.84 \pm 0.12$, and $\gamma = 0.14 \pm 0.04$. Although there is some dispersion and the completeness is very likely small at $\log_{10}M_{star} < 10.0$, Fig. 8 suggests that the relation from Bogdanoska & Burgarella (2020) at $z = 5.0$ is in broad agreement with the data. However, the large number of upper limits at low mass could suggest that the level of the flat relation might be overestimated with respect to the present data. Alternate ways to measure A_{FUV} for low-mass galaxies should be explored, maybe via the Balmer decrements with JWST or with radio data using the radio-to-IR ratio q_{IR} that allows one to constrain the far-IR emission of star-forming galaxies from radio data (e.g., Helou et al. 1985; Delvecchio et al. 2021).

4.3. The $IRX - \beta_{FUV}$ diagram

To estimate the UV slope β_{FUV} , we used the definition given by Calzetti et al. (1994) in the range 125-260 nm within ten selected windows (see their Tab. 2) designed to remove all absorption features and the 217.5 nm dust bump ($\beta_{Calzetti-1994}$) from the fitting procedure. The $IRX - \beta_{FUV}$ is a classical tool to estimate the dust attenuation of galaxies. Fig. 9 shows the location of the galaxies in the IRX versus β_{FUV} diagram. We also show the classical positions assuming a Calzetti law and a small Magellanic cloud (SMC) law. Our galaxies appear to be systematically shifted to the left of the diagram, that is to bluer values of β_{FUV} compared to the locus estimated by Overzier et al. (2010) for galaxies at $z = 0$. This might be related to the evolution of the stellar population at $z \sim 4.5 - 5.0$ as they were younger and bluer (and/or an intrinsic evolution of other parameters similar to the IMF). Age effects were already found at low redshift (e.g., Kong et al. 2004; Boquien et al. 2009).

The IllustrisTNG Project (TNG hereafter: Nelson et al. 2018; Pillepich et al. 2018) is a suite of cosmological simulations for the formation of galaxies. TNG50 does not model dust directly, but Schulz et al. (2020) assume that the diffuse dust content of a galaxy is traced by the gas-phase metal distribution assigned to this galaxy. The dust density distribution is derived from the TNG50 gas density distribution with assumptions on the dust-to-metal ratio, the gas metallicity, the gas temperature, and the

instantaneous SFR. Finally, SKIRT (Baes et al. 2011) is used to model the emission of the galaxies. Their fiducial model is a multicomponent dust mix, which models a composition of graphite, silicate, and polycyclic aromatic hydrocarbon (PAH) grains, with various grain size bins for each grain type which reproduce the properties of Milky Way (MW), large Magellanic cloud (LMC), and SMC type dust. In SKIRT, the dust of the molecular birth clouds mentioned is treated separately from the diffuse ISM dust.

Schulz et al. (2020) used the output of the TNG50 simulation and suggest a redshift-dependent systematic shift toward lower β_{FUV} with increasing redshift modeled by adding a component $\beta_z(z) = 0.142z - 0.081$ to the β_{FUV} value at $z=0$. The trend was calibrated up to $z = 4$. If we extrapolate their trend out to the redshift of our galaxies, the corresponding locus in Fig. 9 would appear too blue when compared to most of our galaxies. In order to extend the redshift range, we computed $\beta_z = \beta - \beta_{Overzier}$ et al. 2010 because Overzier et al. (2010) is the reference at $z = 0$ used by Schulz et al. (2020).

An evolution in redshift of this effect is observationally confirmed. One of the main parameters that can be at the origin of the shift is likely to be the evolution of the stellar population, as mentioned above. So, even though using the redshift as the independent variable might be a simple solution, a more realistic and physical approach should be related to the stellar populations themselves. Schulz et al. (2020) present, in their Figure 7 (middle), the variations of the intrinsic UV slopes β_0 of the galaxy stellar population (i.e., before the attenuation by dust) against their mass weighted mean stellar population ages. This figure shows that β_0 correlates with the stellar population age: the younger the stellar population, the lower β_0 is. From Figure 7 (middle) from Schulz et al. (2020), we measured the mean and uncertainties over each axis of the intrinsic UV-slopes β_0 and of the mass-weighted mean stellar population ages ($age_{M_{star}}$) for each redshift range. CIGALE provides mass-weighted mean stellar population ages for each of the galaxies and for our two best models defined above (i.e., delayed SFH with $\tau = 500$ Myrs plus DL2014 and PL+OT_MBB for the IR emission). These values are plotted in Fig. 10. The average in the four bins of $age_{M_{star}}$ from Schulz et al. (2020) and our data points seem to follow a linear relation. Although the points from Schulz et al. (2020) are not fully compatible with ours, there is a general trend. Statistical tests with the LINMIX library, which uses a hierarchical Bayesian approach for the linear regression with an error in both X and Y (Kelly 2007), suggest that the trend is highly significant (see correlation coefficient in Fig. 10), given the number of points used. The equations in Fig. 10 allow one to quantify this systematic shift along β_{FUV} at large redshift.

4.4. The dust formation rate diagram (DFRD)

Burgarella et al. (2020) and Nanni et al. (2020) built a diagram to follow the evolution of the dust mass called the dust formation rate diagram (DFRD) which shows the specific dust mass ($M_{dust} / M_{star} = sM_{dust}$) versus the specific star formation rate (SFR / $M_{star} = sSFR$). The specific dust mass was already identified by Calura et al. (2017) as a quantity that represents a true measure of how much dust per unit stellar mass survives the various destruction processes in galaxies. However, this is also a quantity that allows one to quantify the various dust formation processes. The interpretation of this DFRD is that galaxies would follow a dust cycle where they start to build their dust grains at high sSFR leading to a fast rise in sM_{dust} . After this phase, the galaxies would reach a maximum in sM_{dust} before losing

their dust grains and going down in the DFRD. At the end of this dust cycle, Burgarella et al. (2020) and Nanni et al. (2020) found that about 80% of the mass fraction of the total baryons had been removed by the outflow and the rest had mainly been destroyed by supernovae (SNe). However, we still have difficulty understanding the evolutionary status of galaxies with very high $sM_{dust} > 0.01$. Calura et al. (2017) propose that spiral galaxies are characterized by a nearly constant sM_{dust} as a function of the stellar mass and cosmic time, whereas proto-spheroids present an early steep increase of the sM_{dust} , which stops at a maximal value and decreases in the latest stages.

We built this same diagram from the large galaxy sample studied in this paper and for our two main models (delayed SFH with $\tau = 500$ Myrs plus DL2014 and PL+OT_MBB for the IR emission). When using the module DL2014 in CIGALE, the dust mass is provided with the models. We note that the models of DL2014 assume an optically thin dust. The CIGALE module casey2012_OT, that is PL+OT_MBB, does not give M_{dust} , and we need to compute it.

The IR SED

$$S_\nu \propto \nu^{\beta_{RJ}} B_\nu(T_{dust})$$

was computed with a modified blackbody

$$B_\nu(T_{dust}) = \frac{2h}{c^2} \frac{\nu^3}{e^{\frac{h\nu}{kT_{dust}}} - 1}$$

and the dust mass was derived with the following formula:

$$M_{dust} = \frac{L_\nu}{4\pi\kappa_\nu B_\nu(T_{dust})}$$

where $\nu = c / \lambda_{200 \mu m}$, h is the Planck constant, and c is the speed of light. We note that the emission of the CMB was neglected given the dust temperatures $T \gtrsim 40$ K found in this paper (da Cunha et al. 2013).

In the models for DL2014, the dust composition (Weingartner & Draine 2001) corresponds to 30% of graphite and 70% of silicate (MgFeSiO₄). We first adopted the constant given in Draine (2003) at $\lambda = 200 \mu m$: $\kappa_0 = 0.637 \text{ m}^2 \text{ kg}^{-1}$ because we also assumed $\lambda_0 = 200 \mu m$, $\kappa_\nu = \kappa_0 (\lambda_0 / \lambda)^\beta = \kappa_0$. When comparing $M_{dust}(\text{DL2014})$ to $M_{dust}(\text{PL+OT_MBB})$, we found the latter to be systematically smaller by a factor of 0.37 ± 0.01 . This was already noticed in several works (Magdis et al. 2013; Santini et al. 2014; Bianchi et al. 2019; Magnelli et al. 2012). The origin of this shift might be found in the single-temperature models that are unable to account for the wide range in the temperature of dust grains that are exposed to different intensities of the interstellar radiation field (see Liang et al. 2019, for a very pedagogical description).

Fig. 11 presents the DFRD with data points color-coded with the parameters age_{main} . Only individual results obtained using DL2014 are shown. However, the trends are also presented for other dust emissions (PL+OT_MBB with various assumptions on κ_0 , as explained below). The lines are based on a fit with only the ALMA-detected objects. We see an age sequence from right to left, that is with decreasing sSFR.

We note that $\kappa_0 = 0.637 \text{ m}^2 \text{ kg}^{-1}$ corresponds to the dust opacity in the models of DL2014. In the early universe, most if not all of the dust could only be produced by SNe (e.g., Burgarella et al. 2020; Nanni et al. 2020). Hirashita et al. (2017) propose values for κ_0 for dust condensed in SNe before reverse shock destruction, $\kappa_{158 \mu m} = 0.557 \text{ m}^2 \text{ kg}^{-1}$, and for dust ejected from SNe after reverse shock destruction, $\kappa_{158 \mu m} = 0.894 \text{ m}^2 \text{ kg}^{-1}$. The dust composition and grain size distribution assumed

in Hirashita et al. (2017) are from Nozawa et al. (2003). After correction to get these dust mass absorption coefficients at $\lambda = 200 \mu\text{m}$ using $\kappa_\nu = \kappa_0 (\lambda_0 / \lambda)^{\beta_{RJ}}$ with β_{RJ} from the SED fitting (Tab. 4), we obtained $\kappa_0 = 0.45$ and $0.72 \text{ m}^2 \text{ kg}^{-1}$. This means that, when adopting the SNe value for κ_0 , the dust masses would be roughly of the same order as PL+OT_MBB with $\kappa_0 = 0.637 \text{ m}^2 \text{ kg}^{-1}$. This is certainly a crucial point: given the age of these galaxies, it is very likely that the dust grains have been produced by SNe. So we could wonder how to reconcile this assumption with the fact that the present models are far from being able to reproduce diagnostic diagrams such as Fig. 11. This point is also debated from a laboratory standpoint. For instance, Fanciullo et al. (2020); Ysard et al. (2019) suggest that current dust masses are overestimated by up to a factor of 10 - 20 or 2 - 5, depending on the assumptions on grain structure (porous or compact, respectively). Laboratory measurements of dust analogs show that FIR opacities, that is to say mass absorption coefficients, are usually higher than the values used in models and that they depend on several parameters, including temperature, composition, shape, and morphology, for instance. This would mean that dust mass estimates may be overestimated. The properties (e.g., dust composition and grain size) are still unknown for galaxies at a very large redshift. This is important when deriving the dust mass (e.g., Ysard et al. 2019; Hirashita et al. 2017; Inoue et al. 2020).

One interesting point, which is beyond of the scope of this work, is related to the nature of objects that are usually considered to belong to another class: the high redshift dusty star-forming galaxies (DSFG) such as ADFS-27 (Riechers et al. 2021) or HFLS3 (Riechers et al. 2013). The very massive and very dusty galaxies have been found in the high redshift universe thanks to wide-field far-IR and submm observations with, for example, the South Pole Telescope or the European Space Agency's Herschel Space Observatory. High redshift DSFGs are at the high mass end, which suggests that they are not similar to the early phases of the SFGs analyzed here. In an attempt to check their location in the DFRD, we added the DSFGs from Tab. 8 to Fig. 12. All of them fall on the same sequence identified for our studied sample; however, they do not show the same stellar mass as our sample. We can wonder whether the stellar mass of these high redshift DSFGs are badly estimated or whether they follow a different path. It should be noticed that CIGALE with similar assumptions on the SFH and on the dust emission has been used for some of these objects, such as ADFS-27.

In Fig. 12, we compare the entire sample with the models built in Burgarella et al. (2020) and in Nanni et al. (2020). The models are fully explained in Nanni et al. (2020). In brief, we performed the calculations for the metal evolution using the One-zone Model for the Evolution of GALaxies (OMEGA) code (Côté et al. 2017). We assumed the metal yields for type II SNe from Kobayashi et al. (2006) computed up to $40 M_\odot$, and from the FRUITY database for low-mass stars with $M > 1.3 M_\odot$ evolving through the thermally pulsing AGB phase and developing stellar winds (Cristallo et al. 2011, Piersanti et al. 2013, Cristallo et al. 2015). The yields for population III stars are from Heger & Woosley (2010) and are limited to the mass range $10 < M/M_\odot < 30$ in OMEGA. Dust removal from the galaxy through galactic outflow follows a rate proportional to the SFR through the "mass-loading factor": $\text{ML} \times \text{SFR}$. This assumes that the galactic outflow is generated by the feedback of stars on the gas in the ISM (e.g., Murray et al. 2005). Two kinds of IMFs were tested: top-heavy IMFs and a Chabrier IMF. We assume that a fraction of silicates (olivine and pyroxene), iron, and carbon grains ejected in the ISM are condensed. The best models selected by

Burgarella et al. (2020) generally agree with the Alpine sample. Only one object (HZ9 at $\text{sSFR} \sim 5 - 6 \times 10^{-8} \text{ yr}^{-1}$) lies at high sSFR. This is consistent with a fast evolution of these young objects, regardless of their sM_{dust} . With the present data, we cannot rule out that the trend could keep rising to the right of the diagram. Galaxies have to start building dust grains early in their lifetime, at $\log_{10} \text{ sSFR} \geq 10^{-8} - 10^{-7} \text{ yr}^{-1}$, to the right of the DFRD. It therefore seems important to measure dust and stellar masses for galaxies at high sSFR and young ages to locate the locus of this rising sM_{dust} and thus bring some observational data to constrain the models.

5. Conclusions

This paper studies a sample of star-forming galaxies observed with ALMA in the redshift range $4.5 \lesssim z \lesssim 6.2$. Some of them, detected in the continuum with ALMA, were used to build a composite IR SED covering a large wavelength range from about $15 \mu\text{m}$ to $218 \mu\text{m}$. Using CIGALE, we modeled the IR composite template and derived a set of physical properties. Building on the assumption that this IR composite template is valid for an ensemble of galaxies selected in the same way, such as ALPINE's SFGs and LBGs, we use it to fit the SEDs of the ALPINE sample plus the sample of LBGs from Burgarella et al. (2020) and Nanni et al. (2020) from the far-UV to the submm ranges.

The following results were found:

- We built a unique $z > 4$ IR SED. It is compatible with the ALPINE sample completed with galaxies from Burgarella et al. (2020) plus the $z \sim 4.5$ and $z \sim 5.5$ stacks from Bethermin et al. (2020). We provide a table to the readers with the raw composite IR SED and the modeled SEDs.
- Except for an SFH based on a delayed with a final burst history, all other SFHs (constant, delayed with $\tau_{\text{main}} = 500$ Myrs, and delayed with several τ_{main}) are in agreement with the data. For simplicity, we selected the delayed SFH with $\tau_{\text{main}} = 500$ Myrs.
- We checked the position of the sample in the SFR versus M_{star} diagram. The objects in the sample follow the same trend as those previously derived in papers at the same redshift.
- When comparing the position of the sample with the evolution in redshift of the IRX versus M_{star} relation found by Bogdanoska & Burgarella (2020) at $z \sim 4.5$ and at $z \sim 5.5$, we found a reasonable agreement. This agreement especially holds at $z \sim 5.5$. However, the absolute level of this flat relation must be reevaluated using detections of low-mass galaxies.
- The sample studied in this paper was placed in the IRX versus β_{FUV} diagram. An evolution in age is observed with younger galaxies having bluer β_{FUV} .
- Moreover, our sample was found to be shifted to bluer β_{FUV} with respect to a $z = 0$ reference. We modeled this evolution with the mass-weighted age and provide an equation that allows one to predict the position of the sequence as a function of the redshift.
- We plotted our galaxies in the DFRD ($M_{\text{dust}}/M_{\text{star}}$ versus $\text{SFR}/M_{\text{star}}$, DFRD). The objects form a sequence that can be described by evolution in various time-dependent parameters, and more specifically the age of the stellar populations and the stellar mass. This suggests that the sequence is due to the evolution of the galaxies over cosmic time.
- The models built by Burgarella et al. (2020); Nanni et al. (2020) are generally in agreement with the data, although the sample is much larger than in these previous papers.

id	z	μ	M_{dust}	M_{dust_err}	M_{star}	M_{star_err}	M_{gas}	M_{gas_err}	SFR	SFR_err	f_{gas}^*	ref
ADFS-27	5.7	1.0	4.2E9	0.4E9	2.1E11	0.6E11	2.1E11	0.2E11	2380	230	0.50	¹
ADFS-27 N	5.7	1.0	2.6E9	0.4E9	1.6E11	1.3E11	1.2E11	0.1E11	1330	130	0.43	¹
ADFS-27 S	5.7	1.0	1.5E9	0.2E9	4.6E10	1.5E10	9.4E10	0.8E10	1050	110	0.66	¹
HFLS-3	6.3	2.2	1.3E9	0.3E9	3.7E10	1.1E10 [#]	1.0E11	0.1E11	2900	180	0.73	^{2,3}
SPT 0311-58 [§]	6.9	2.0	6.1E9	3.5E9	1.1E11	0.5E11	6.4E11	3.7E11	7082	3967	0.85	^{4,5}
SPT 0311-58W	6.9	2.2	5.5E9	3.5E9	6.6E10	4.4E10	5.9E11	3.7E11	6380	3960	0.90	^{4,5}
SPT 0311-58E	6.9	1.3	5.2E8	2.6E8	4.6E10	2.0E10	5.2E10	2.6E10	702	228	0.53	^{4,5}
GN10	5.3	1.0	1.1E9	4.4E8	1.2E11	0.6E10	7.1E10	0.9E10	1030	190	0.37	⁶

Table 8: Physical parameters for the sample of high redshift dusty star-forming galaxies. We note that the parameters were not corrected for the gravitational magnification. ¹: Riechers et al. (2021), ²: Riechers et al. (2013), ³ Cooray2014, ⁴ Strandet2017; ⁵ Marrone2018, ⁶: Riechers et al. (2020). * $f_{gas} = M_{gas}/(M_{gas}+M_{star})$ were computed from the listed M_{gas} and M_{star} values. [#] No error quoted, we assume 30%. [§] The parameters for SPT031158 are the sum of the two components (W & E).

– High redshift, high mass DSFGs over-plotted in the DFRD are found on the same sequence followed by our sample. However, the stellar mass estimated for these high redshift DSFGs are larger than the one found at the same locus for our sample. Uncertainties on the stellar mass of these objects are notoriously high because the stellar emission is faint, but the disagreement seems large. Better estimates of their stellar masses should be available if they are observed with JWST.

Acknowledgements. This program receives funding from the CNRS national program Cosmology and Galaxies. D.R. acknowledges support from the National Science Foundation under grant No. AST-1910107. D.R. also acknowledges support from the Alexander von Humboldt Foundation through a Humboldt Research Fellowship for Experienced Researchers. M.T. acknowledges the support from grant PRIN MIUR 2017 20173ML3WW 001. A.N. acknowledges support from the Narodowe Centrum Nauki (UMO-2018/30/E/ST9/00082 and UMO-2020/38/E/ST9/00077). G.C.J. acknowledges ERC Advanced Grant 695671 “QUENCH” and support by the Science and Technology Facilities Council (STFC). Y.F. further acknowledges support from NAOJ ALMA Scientific Research Grant number 2020-16B. M.R. acknowledges support from the Narodowe Centrum Nauki (UMO-2020/38/E/ST9/00077). Médéric Boquien gratefully acknowledges support by the ANID BASAL project FB210003 and from the FONDECYT regular grant 1211000. E.I. acknowledges partial support from FONDECYT through grant N° 1171710

References

- Álvarez-Márquez, J., Burgarella, D., Buat, V., Ilbert, O., & Pérez-González, P. G. 2019, *A&A*, 630, A153
- Álvarez-Márquez, J., Burgarella, D., Heinis, S., et al. 2016, *A&A*, 587, A122
- Arata, S., Yajima, H., Nagamine, K., Abe, M., & Khochfar, S. 2020, *MNRAS*, 498, 5541
- Aretxaga, I., Wilson, G. W., Aguilar, E., et al. 2011, *MNRAS*, 415, 3831
- Baes, M., Verstackpen, J., De Looze, I., et al. 2011, *ApJS*, 196, 22
- Bakk, T. J. L. C., Sommovigo, L., Carniani, S., et al. 2021, *MNRAS*, 508, L58
- Bellstedt, S., Robotham, A. S. G., Driver, S. P., et al. 2021, *MNRAS*, 503, 3309
- Bendo, G. J., Joseph, R. D., Wells, M., et al. 2003, *AJ*, 125, 2361
- Bernhard, E., Béthermin, M., Sargent, M., et al. 2014, *MNRAS*, 442, 509
- Béthermin, M., Fudamoto, Y., Ginolfi, M., et al. 2020, *arXiv:2002.00962 [astro-ph]*
- Bianchi, S., Casasola, V., Baes, M., et al. 2019, *A&A*, 631, A102
- Bogdanoska, J. & Burgarella, D. 2020, *MNRAS*, 496, 5341
- Boquien, M., Burgarella, D., Roehly, Y., et al. 2019, *A&A*, 622, A103
- Boquien, M., Calzetti, D., Kennicutt, R., et al. 2009, *ApJ*, 706, 553
- Bouwens, R. J., Aravena, M., Decarli, R., et al. 2016, *ApJ*, 833, 72
- Bruzual, G. & Charlot, S. 2003, *MNRAS*, 344, 1000
- Buat, V., Takeuchi, T. T., Burgarella, D., Giovannoli, E., & Murata, K. L. 2009, *A&A*, 507, 693
- Burgarella, D., Buat, V., Gruppioni, C., et al. 2013, *A&A*, 554, A70
- Burgarella, D., Nanni, A., Hirashita, H., et al. 2020, *A&A*, 637, A32
- Calura, F., Pozzi, F., Cresci, G., et al. 2017, *MNRAS*, 465, 54
- Calzetti, D., Armus, L., Bohlin, R. C., et al. 2000, *ApJ*, 533, 682
- Calzetti, D., Kinney, A. L., & Storchi-Bergmann, T. 1994, *ApJ*, 429, 582
- Capak, P. L., Carilli, C., Jones, G., et al. 2015, *Nature*, 522, 455
- Carvajal, R., Bauer, F. E., Bouwens, R. J., et al. 2020, *A&A*, 633, A160
- Casey, C. M. 2012, *MNRAS*, 425, 3094
- Casey, C. M., Chen, C.-C., Cowie, L. L., et al. 2013, *MNRAS*, 436, 1919
- Castellano, M., Sommariva, V., Fontana, A., et al. 2014, *A&A*, 566, A19
- Chabrier, G. 2003, *PASP*, 115, 763
- Ciesla, L., Boquien, M., Boselli, A., et al. 2014, *A&A*, 565, A128
- Cormier, D., Abel, N. P., Hony, S., et al. 2019, *A&A*, 626, A23
- Cortese, L., Boselli, A., Franzetti, P., et al. 2008, *MNRAS*, 386, 1157
- Côté, B., O’Shea, W., Ritter, C., Herwig, F., & Venn, K. A. 2017, *ApJ*, 835, 128
- Cousin, M., Buat, V., Lagache, G., & Béthermin, M. 2019, *Astronomy and Astrophysics*, 627, A132
- Cristallo, S., Piersanti, L., Straniero, O., et al. 2011, *ApJS*, 197, 17
- Cristallo, S., Straniero, O., Piersanti, L., & Gobrecht, D. 2015, *ApJS*, 219, 40
- Cucciati, O., Tresse, L., Ilbert, O., et al. 2012, *A&A*, 539, A31
- Cunningham, D. J. M., Chapman, S. C., Aravena, M., et al. 2020, *MNRAS*, 494, 4090
- da Cunha, E., Groves, B., Walter, F., et al. 2013, *ApJ*, 766, 13
- De Brueck, C., Weiß, A., Béthermin, M., et al. 2019, *A&A*, 631, A167
- Delvecchio, I., Daddi, E., Sargent, M. T., et al. 2021, *A&A*, 647, A123
- Donnari, M., Pillepich, A., Nelson, D., et al. 2019, *MNRAS*, 485, 4817
- Douglas, L. S., Bremer, M. N., Lehnert, M. D., Stanway, E. R., & Milvang-Jensen, B. 2010, *MNRAS*, 409, 1155
- Draine, B. T. 2003, *ARA&A*, 41, 241
- Draine, B. T., Aniano, G., Krause, O., et al. 2014, *ApJ*, 780, 172
- Faisst, A. L., Capak, P. L., Yan, L., et al. 2017, *ApJ*, 847, 21
- Faisst, A. L., Fudamoto, Y., Oesch, P. A., et al. 2020, *MNRAS*, 498, 4192
- Faisst, A. L., Schaerer, D., Lemaux, B. C., et al. 2020, *The Astrophysical Journal Supplement Series*, 247, 61
- Fanciullo, L., Kemper, F., Scicluna, P., Dharmawardena, T. E., & Srinivasan, S. 2020, *MNRAS*, 499, 4666
- Fernández-Ontiveros, J. A., Spinoglio, L., Pereira-Santaella, M., et al. 2016, *ApJS*, 226, 19
- Fudamoto, Y., Oesch, P. A., Faisst, A., et al. 2020, *A&A*, 643, A4
- Fujimoto, S., Silverman, J. D., Béthermin, M., et al. 2020, *ApJ*, 900, 1
- Galamez, M., Kennicutt, R. C., Albrecht, M., et al. 2012, *MNRAS*, 425, 763
- Giacconi, R., Zirm, A., Wang, J., et al. 2002, *VizieR Online Data Catalog*, 213
- Grogan, N. A., Kocevski, D. D., Faber, S. M., et al. 2011, *ApJS*, 197, 35
- Gruppioni, C., Pozzi, F., Rodighiero, G., et al. 2013, *MNRAS*, 432, 23
- Harikane, Y., Ouchi, M., Inoue, A. K., et al. 2020, *ApJ*, 896, 93
- Harikane, Y., Ouchi, M., Yuma, S., et al. 2014, *ApJ*, 794, 129
- Hashimoto, T., Inoue, A. K., Mawatari, K., et al. 2019, *PASJ*, 71, 71
- Hashimoto, T., Laporte, N., Mawatari, K., et al. 2018, *Nature*, 557, 392
- Heger, A. & Woosley, S. E. 2010, *ApJ*, 724, 341
- Helou, G., Soifer, B. T., & Rowan-Robinson, M. 1985, *ApJ*, 298, L7
- Hirashita, H., Burgarella, D., & Bouwens, R. J. 2017, *MNRAS*, 472, 4587
- Hunt, L. K., Testi, L., Casasola, V., et al. 2014, *A&A*, 561, A49
- Inoue, A. K., Hashimoto, T., Chihara, H., & Koike, C. 2020, *MNRAS*, 495, 1577
- Inoue, A. K., Tamura, Y., Matsuo, H., et al. 2016, *Science*, 352, 1559
- Jones, G. C., Maiolino, R., Caselli, P., & Carniani, S. 2020, *MNRAS*, 498, 4109
- Juvela, M., Montillaud, J., Ysard, N., & Lunttila, T. 2013, *A&A*, 556, A63
- Kass, R. E. & Raftery, A. E. 1995, *Journal of the American Statistical Association*, 90, 773
- Kelly, B. C. 2007, *ApJ*, 665, 1489
- Khusanova, Y., Béthermin, M., Le Fèvre, O., et al. 2021, *A&A*, 649, A152
- Kobayashi, C., Umeda, H., Nomoto, K., Tominaga, N., & Ohkubo, T. 2006, *ApJ*, 653, 1145
- Koekemoer, A. M., Faber, S. M., Ferguson, H. C., et al. 2011, *ApJS*, 197, 36
- Komatsu, E., Smith, K. M., Dunkley, J., et al. 2011, *ApJS*, 192, 18
- Kong, X., Charlot, S., Brinchmann, J., & Fall, S. M. 2004, *MNRAS*, 349, 769
- Koprowski, M. P., Coppin, K. E. K., Geach, J. E., et al. 2020, *MNRAS*, 492, 4927
- Lagache, G., Cousin, M., & Chatzikos, M. 2018, *A&A*, 609, A130
- Laporte, N., Katz, H., Ellis, R. S., et al. 2019, *MNRAS*, 487, L81
- Le Fèvre, O., Béthermin, M., Faisst, A., et al. 2020, *A&A*, 643, A1

- Leitherer, C., Calzetti, D., & Martins, L. P. 2002, *ApJ*, 574, 114
- Liang, L., Feldmann, R., Kereš, D., et al. 2019, *MNRAS*, 489, 1397
- Lutz, D., Poglitsch, A., Altieri, B., et al. 2011, *A&A*, 532, A90
- Ma, X., Hopkins, P. F., Faucher-Giguère, C.-A., et al. 2016, *MNRAS*, 456, 2140
- Madau, P. & Dickinson, M. 2014, *ARA&A*, 52, 415
- Madau, P., Ferguson, H. C., Dickinson, M. E., et al. 1996, *MNRAS*, 283, 1388
- Madden, S. C., Rémy-Ruyer, A., Galametz, M., et al. 2013, *PASP*, 125, 600
- Magdis, G. E., Rigopoulou, D., Helou, G., et al. 2013, *A&A*, 558, A136
- Magnelli, B., Lutz, D., Santini, P., et al. 2012, *A&A*, 539, A155
- McLure, R. J., Dunlop, J. S., Cullen, F., et al. 2018, *MNRAS*, 476, 3991
- Murray, N., Quataert, E., & Thompson, T. A. 2005, *ApJ*, 618, 569
- Nanni, A., Burgarella, D., Theulé, P., Côté, B., & Hirashita, H. 2020, *A&A*, submitted
- Nelson, D., Pillepich, A., Springel, V., et al. 2018, *MNRAS*, 475, 624
- Nozawa, T., Kozasa, T., Umeda, H., Maeda, K., & Nomoto, K. 2003, *ApJ*, 598, 785
- O’Halloran, B., Galametz, M., Madden, S. C., et al. 2010, *A&A*, 518, L58
- Oliver, S. J., Bock, J., Altieri, B., et al. 2012, *MNRAS*, 424, 1614
- Ouchi, M., Yamada, T., Kawai, H., & Ohta, K. 1999, *ApJ*, 517, L19
- Overzier, R. A., Heckman, T. M., Schiminovich, D., et al. 2010, *ApJ*, 710, 979
- Pavesi, R., Riechers, D. A., Capak, P. L., et al. 2016, *ApJ*, 832, 151
- Pavesi, R., Riechers, D. A., Faisst, A. L., Stacey, G. J., & Capak, P. L. 2019, *ApJ*, 882, 168
- Pearson, E. A., Eales, S., Dunne, L., et al. 2013, *MNRAS*, 435, 2753
- Pearson, W. J., Wang, L., Hurley, P. D., et al. 2018, *A&A*, 615, A146
- Piersanti, L., Cristallo, S., & Straniero, O. 2013, *ApJ*, 774, 98
- Pilbratt, G. L., Riedinger, J. R., Passvogel, T., et al. 2010, *A&A*, 518, L1
- Pillepich, A., Nelson, D., Hernquist, L., et al. 2018, *MNRAS*, 475, 648
- Pozzi, F., Calura, F., Fudamoto, Y., et al. 2021, *A&A*, 653, A84
- Raftery, A. E. 1998, Bayes Factors and BIC: Comment on Weakliem
- Riechers, D. A., Bradford, C. M., Clements, D. L., et al. 2013, *Nature*, 496, 329
- Riechers, D. A., Hodge, J. A., Pavesi, R., et al. 2020, *ApJ*, 895, 81
- Riechers, D. A., Nayyeri, H., Burgarella, D., et al. 2021, *ApJ*, 907, 62
- Rodighiero, G., Daddi, E., Baronchelli, I., et al. 2011, *ApJ*, 739, L40
- Salim, S., Lee, J. C., Janowiecki, S., et al. 2016, *The Astrophysical Journal Supplement Series*, 227, 2
- Santini, P., Maiolino, R., Magnelli, B., et al. 2014, *A&A*, 562, A30
- Schaerer, D., Ginolfi, M., Béthermin, M., et al. 2020, *A&A*, 643, A3
- Schulz, S., Popping, G., Pillepich, A., et al. 2020, *MNRAS*, 497, 4773
- Scoville, N., Aussel, H., Brusa, M., et al. 2007, *The Astrophysical Journal Supplement Series*, 172, 1
- Scoville, N., Sheth, K., Aussel, H., et al. 2016, *ApJ*, 820, 83
- Shapley, A. E., Steidel, C. C., Pettini, M., & Adelberger, K. L. 2003, *ApJ*, 588, 65
- Sherman, S., Jogee, S., Florez, J., et al. 2021, *MNRAS*, 505, 947
- Speagle, J. S., Steinhardt, C. L., Capak, P. L., & Silverman, J. D. 2014, *The Astrophysical Journal Supplement Series*, 214, 15
- Sugahara, Y., Inoue, A. K., Hashimoto, T., et al. 2021, *arXiv e-prints*, arXiv:2104.02201
- Tabatabaei, F. S., Braine, J., Xilouris, E. M., et al. 2014, *A&A*, 561, A95
- Takeuchi, T. T., Buat, V., Heinis, S., et al. 2010, *A&A*, 514, A4
- Tibbs, C. T., Israel, F. P., Laureijs, R. J., et al. 2018, *MNRAS*, 477, 4968
- Volinsky, Christopher, T. 1997, PhD thesis, University of Washington
- Weingartner, J. C. & Draine, B. T. 2001, *ApJ*, 548, 296
- Willott, C. J., Carilli, C. L., Wagg, J., & Wang, R. 2015, *ApJ*, 807, 180
- Witt, A. N. & Gordon, K. D. 2000, *ApJ*, 528, 799
- Xu, C. K., Shupe, D., Buat, V., et al. 2007, *ApJS*, 173, 432
- Ysard, N., Koehler, M., Jimenez-Serra, I., Jones, A. P., & Verstraete, L. 2019, *A&A*, 631, A88
- Yuan, F.-T., Burgarella, D., Corre, D., et al. 2019, *A&A*, 631, A123

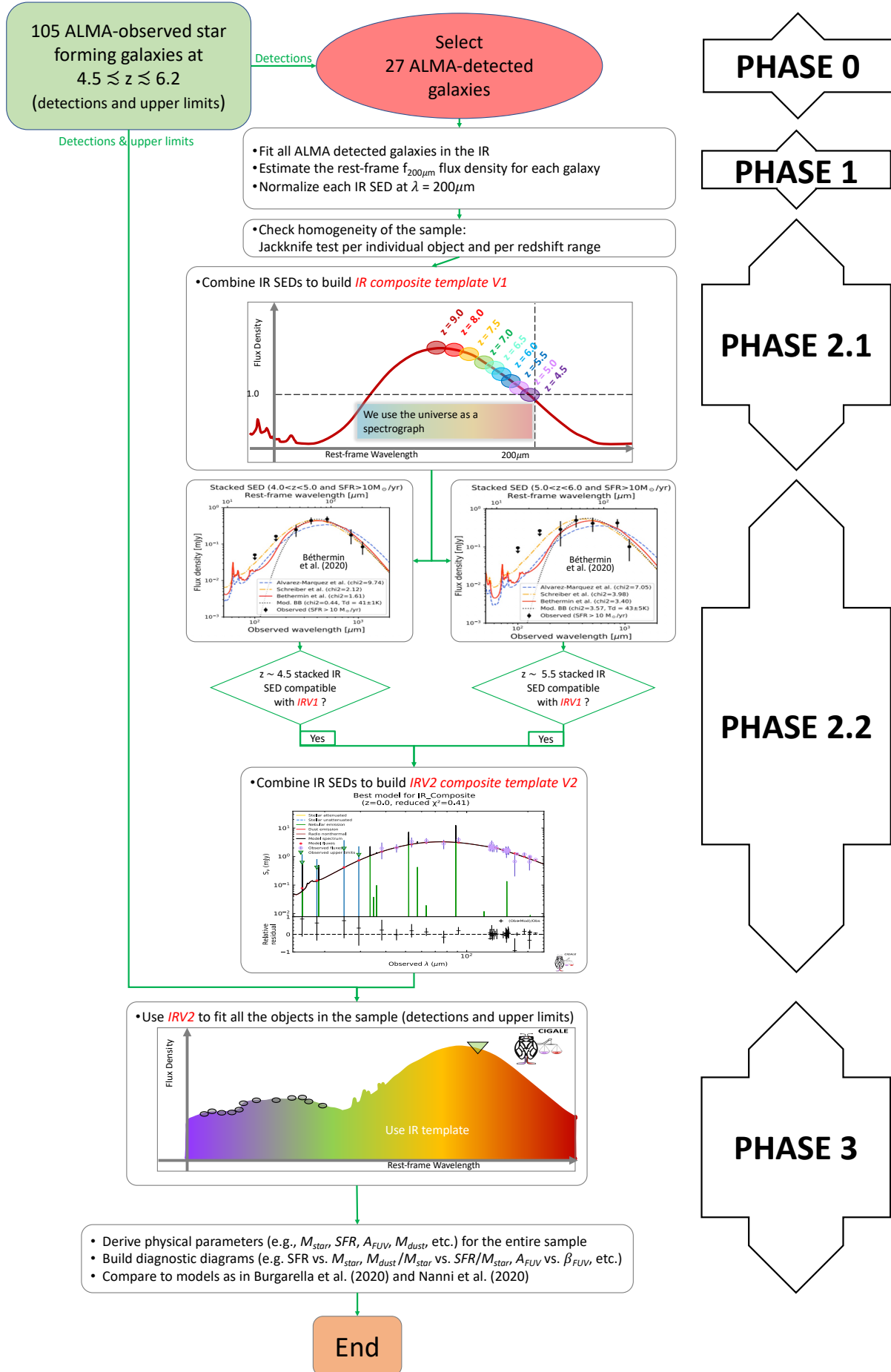


Fig. 1. Flow chart of the process followed to build the composite IR SED for the Hiz-SFGs sample. The various phases of this process are shown on the right side of the figures. They are also described in more detail in the text (see Sect. 3) In the first phase, we selected only ALMA-detected objects to build the first IR template (IRV1). Next, we added the data from the $z \sim 4.5$ and ~ 5.5 stacks from Bethermin et al. (2020) to build the second and final IR template (IRV2). Adding UV and optical data to IRV2, we fit the entire (detected and upper limits) sample.

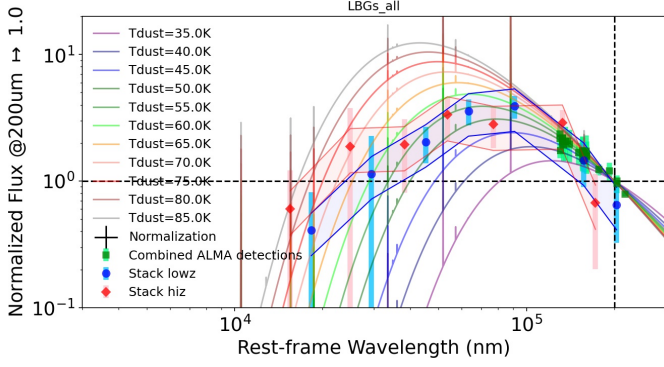


Fig. 2: IR combined SED built from the ALMA-detected objects from the ALPINE sample, from Burgarella et al. (2020), and with the two stacks from Bethermin et al. (2020) and the associated uncertainty regions. We note that the four left-most points for the stacks are upper limits, as shown by the error bars reaching the bottom of the figure. The SEDs corresponding to optically thin modified black bodies are superimposed to the observed SEDs. Qualitatively, we can see that the IR-combined SED seems to be in agreement with greenish modified black-body SEDs, that is $T_{dust} \sim 50 - 60\text{K}$. A qualitative analysis is performed later in this paper.

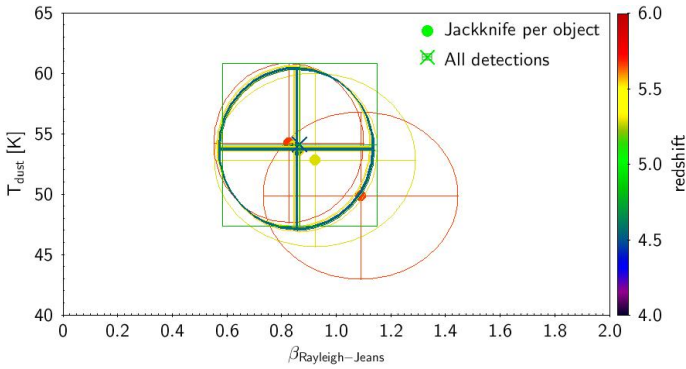


Fig. 3: Degeneracies in T_{dust} and β_{RJ} . The knife jacking method allowed us to estimate whether the characteristics of the dust emission, i.e., T_{dust} and β_{RJ} , vary when removing and adding back individual galaxies from the sample used to build the composite template. The ellipses show the uncertainties. The outlier point at $\beta_{RJ} \sim 1.1$ and $T_{dust} \sim 51\text{K}$ was obtained when taking off HZ10 at $z=5.659$ with five pieces of data in the far-IR+submm range. Only when removing it did the average locus move to slightly larger values of β_{RJ} , but with larger uncertainties.

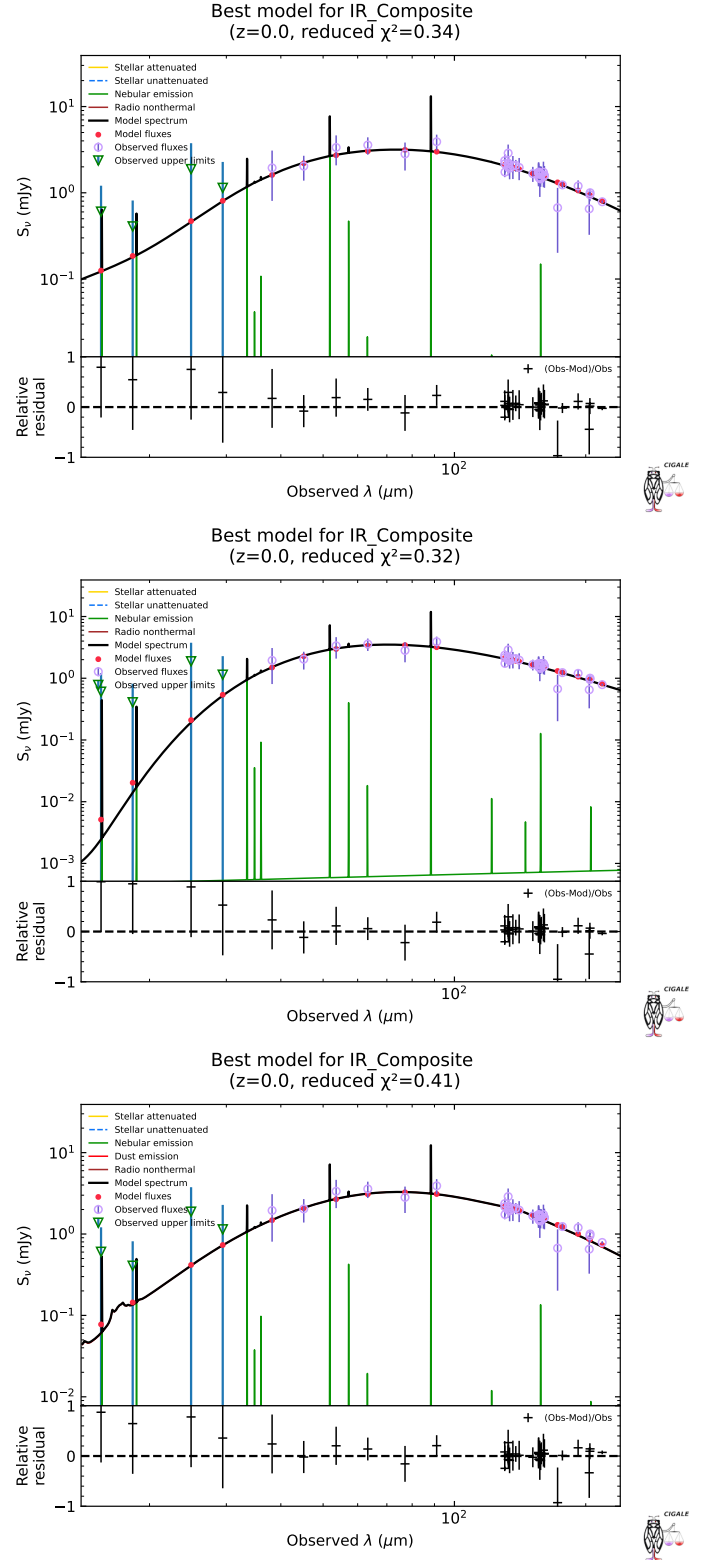


Fig. 4: Comparison of the various fits of the IR composite SED built with data from Burgarella et al. (2020), from ALPINE, and from the $z \sim 4.5$ and $z \sim 5.5$ stacks from Bethermin et al. (2020). Top: Fit with a modified general blackbody and power law in the mid-IR as in Casey et al. (2012). Middle: Fit with an optically thin modified blackbody and power law in the mid-IR as in Casey et al. (2012). Bottom: Fit with a model from Draine & Li (2014). The fits are all statistically equivalently good with reduced $\chi^2 \approx 0.3 - 0.4$.

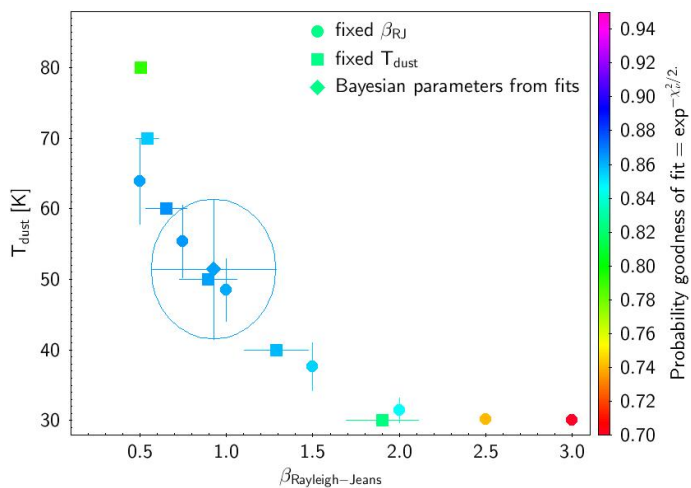


Fig. 5: Results of the tests on the determination of T_{dust} and β_{RJ} and their possible degeneracy are shown here. Dots show the evolution of T_{dust} when β_{RJ} was fixed during the fits. Boxes show the evolution of β_{RJ} when T_{dust} was fixed during the fits. Finally, the diamond symbol shows the result and uncertainties on both axes when T_{dust} and β_{RJ} are both free. The color coding indicates the level of the goodness of fit.

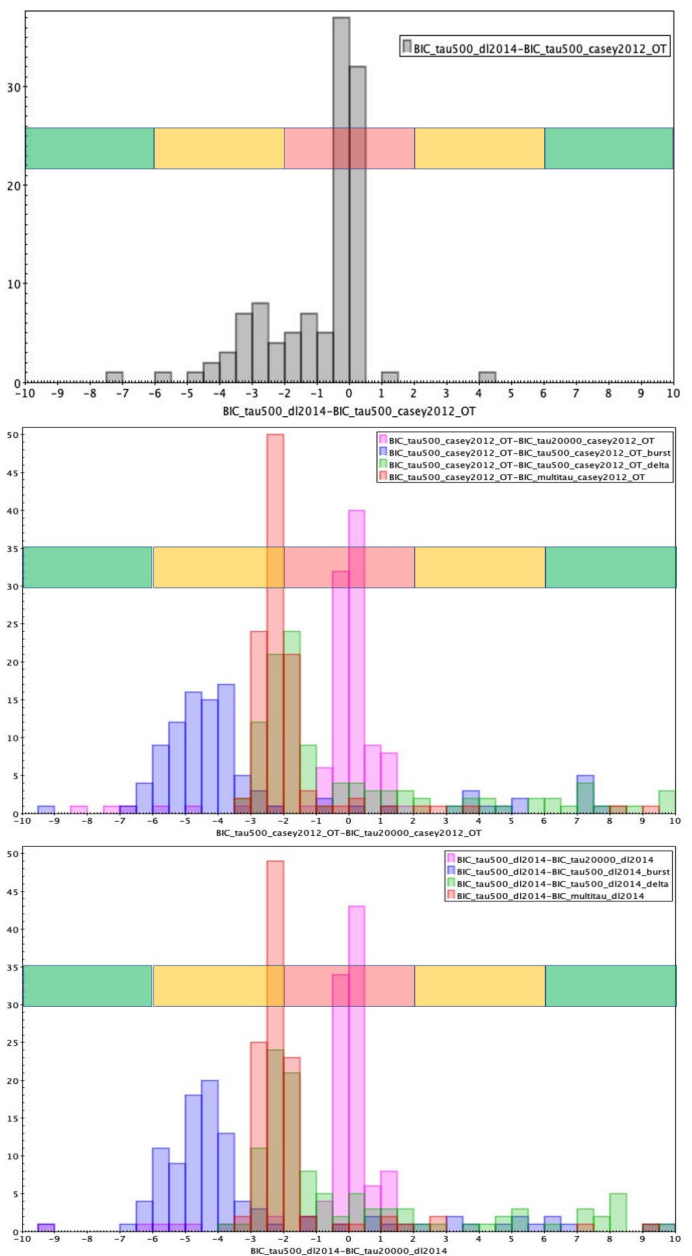


Fig. 6: Result of the ΔBIC test on our sample of Hiz-SFGs. A delayed SFH without a burst and $\tau_{main} = 500$ Myrs is labeled as "tau500". With an additional burst at the end of the SFH, it is labeled as "burst". A constant SFH without a burst and $\tau_{main} = 20$ Gyrs is labeled as "tau20000". And when several τ_{main} could be selected in the SED fitting, it is labeled as "multitau" in the legend. Top: ΔBIC test that compares the influence of the DL2014 model and the PL+OT_MBB dust emissions in building the IR template. Center: ΔBIC test on the SFH assuming the PL+OT_MBB for the IR template. Bottom: ΔBIC test on the SFH assuming the DL2014 model for the IR template. The color band allows one to interpret the results of the evidence (ΔBIC) against the model with the higher BIC: red means "faint evidence," orange means "positive evidence," and green mean "strong evidence." We do not see any strong evidence that DL2014 or PL+OT_MBB are better for fitting the data. An SFH that includes a burst is positively ruled out, while a delayed SFH with $\tau = 500$ Myrs is weakly favored.

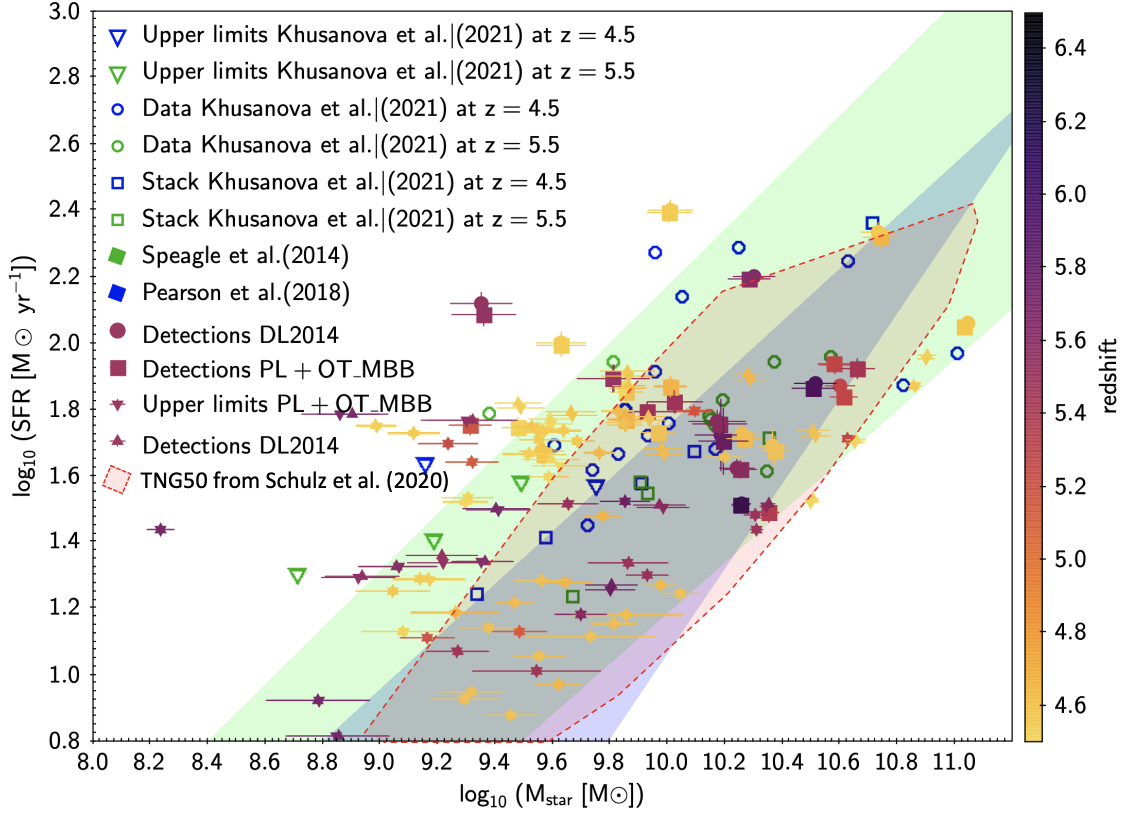


Fig. 7: In the $\log_{10}(\text{SFR})$ vs. $\log_{10}(M_{\text{star}})$ diagram, the main part of the sample is found within the limits for the fits of the main sequence at $z = 5.0$ by Speagle et al. (2014) (green shading), by Pearson et al. (2018) at $z \sim 5.2$ (purple shading), and by Faisst et al. (2020), who found that the galaxies are in agreement with Speagle et al. (2014). It is important to note, however, that some of our objects are at redshifts larger than the 4.5 - 5.6 ALPINE sample (see color code of the markers). For Speagle et al. (2014), we used the “mixed” (preferred fit) function (as defined by Speagle et al. (2014)). The results from the two fits with DL2014 and PL+OT_MBB are presented. The two types of dust emission do not significantly modify the location of the points in the diagram. Detections are shown as dots and boxes and upper limits are shown as downward- and upward-pointing triangles. The uncertainty range for upper limits extends to the bottom of the plot. In addition to having mainly upper limits, at $\log_{10}(M_{\text{star}}) < 9.5$, the sample is very likely incomplete which means that it is difficult to estimate a trend from these data over the entire mass range. We also added the objects and stacks from Khusanova et al. (2021) with open markers. Finally, the selection of TNG50 galaxies used in Schulz et al. (2020) is also provided (red-shaded area).

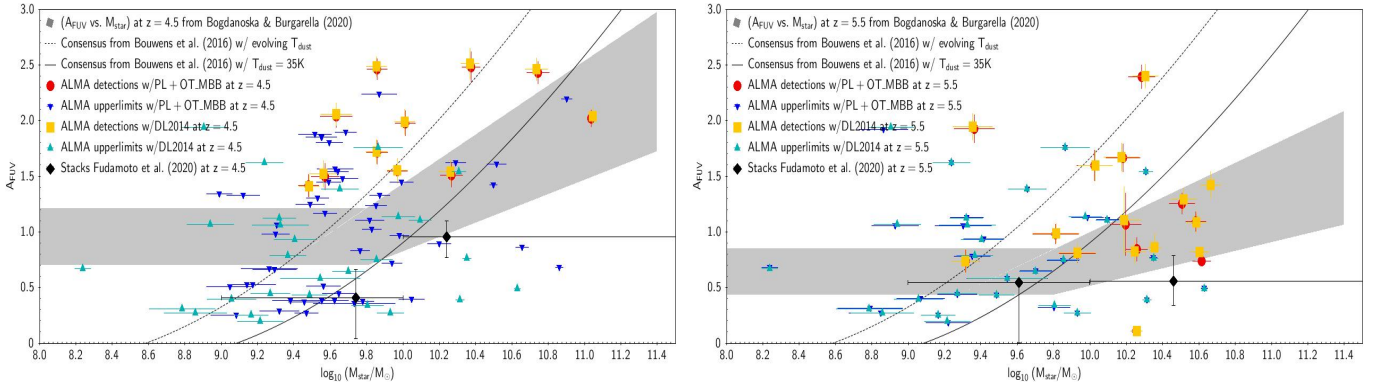


Fig. 8: $A_{FUV} - M_{\text{star}}$ diagram at $z \sim 4.5$ (left) and $z \sim 5.5$ (right). The gray areas correspond to the expected relation at $z = 4.5$ and 5.5 from Bogdanoska & Burgarella (2020). This relation was formed by a broken line, which is flat at $\log_{10} M_{\text{star}} \leq 9.8$ and rises at $\log_{10}(M_{\text{star}}) > 9.8$. The ALPINE data are very dispersed at $z \sim 4.5$, while this flatness is supported by the data at $z \sim 5.5$. The conversion from IRX to A_{FUV} is from Burgarella et al. (2005): $A_{FUV} = -0.028 [\log_{10}(\text{IRX})]^3 + 0.392 [\log_{10}(\text{IRX})]^2 + 1.094 [\log_{10}(\text{IRX})] + 0.5$.

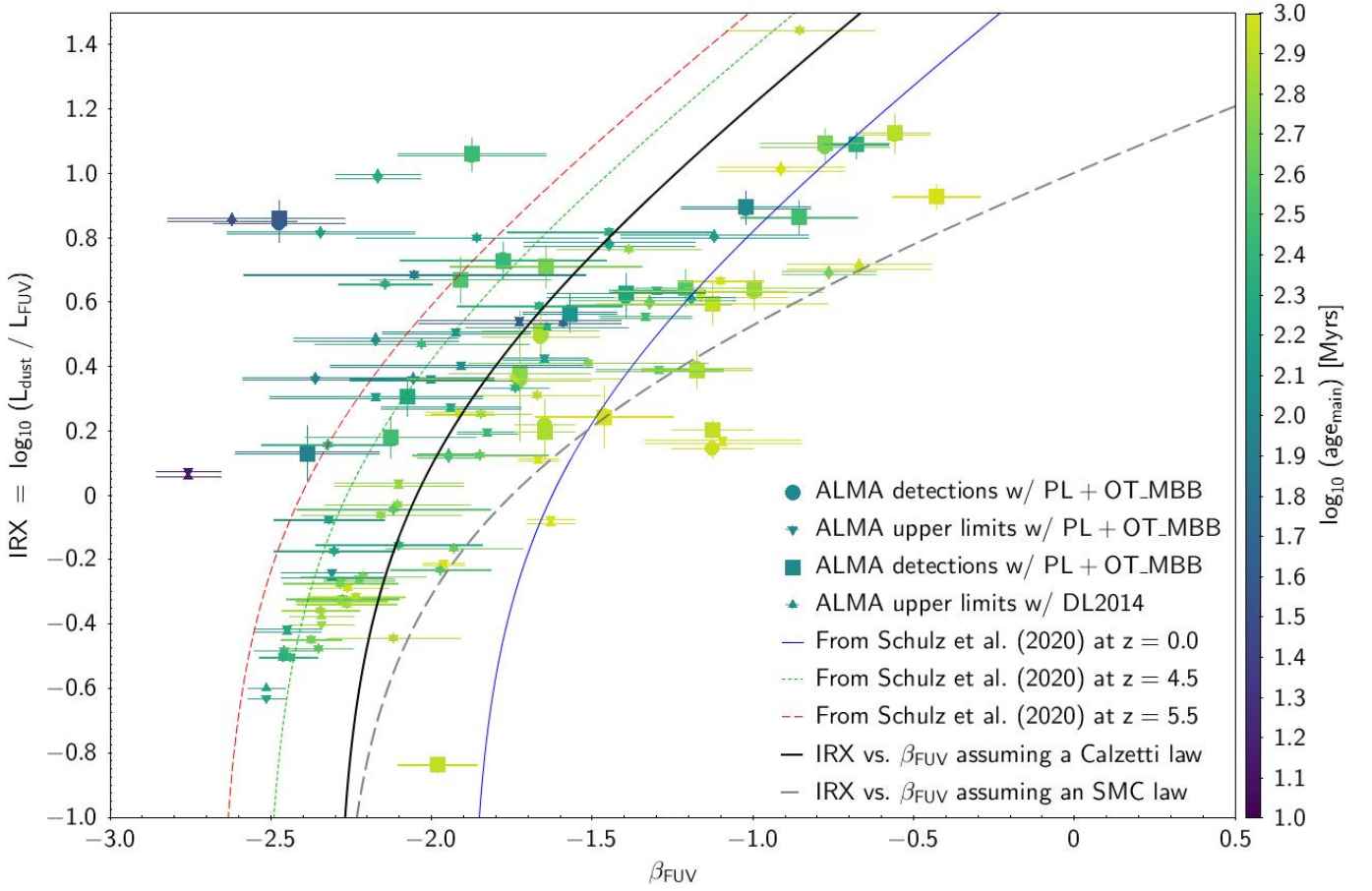


Fig. 9: IRX - β_{FUV} diagram. IRX values were estimated with CIGALE and β_{FUV} were fitted on the data directly. They are not model-dependant. The black continuous line corresponds to the original Calzetti law, under the assumption that the underlying dust curve follows the Calzetti et al. (2000) attenuation. The dashed line to the predicted law assumes the SMC extinction law (e.g., Gordon et al. 2003). Both are from McLure et al. (2018). The color of the symbols are related to the axis to the right of the figure, the age of the stellar population. Both results with dust emission, DL2014 and PL+OT_MBB, are presented with different symbols with ALMA upper limits and ALMA detections. In the figures, we also plotted the laws from Schulz et al. (2020) at $z = 0.0$ (blue continuous line), 4.5 (green dotted line), and 5.5 (red dashed line). A comparison with the IRX - β_{FUV} plot in Fudamoto et al. (2020) with the same sample suggests that our (especially ALMA-detected) galaxies extend less to very blue β_{FUV} . This is mainly true for the subsample of galaxies not detected in continuum with ALMA. This is probably due to two effects: first, in Fudamoto et al. (2020), 3σ upper limits are plotted. Another possible effect could be because we used a unique IR composite template in the SED fitting, which reduces the uncertainties on L_{dust} .

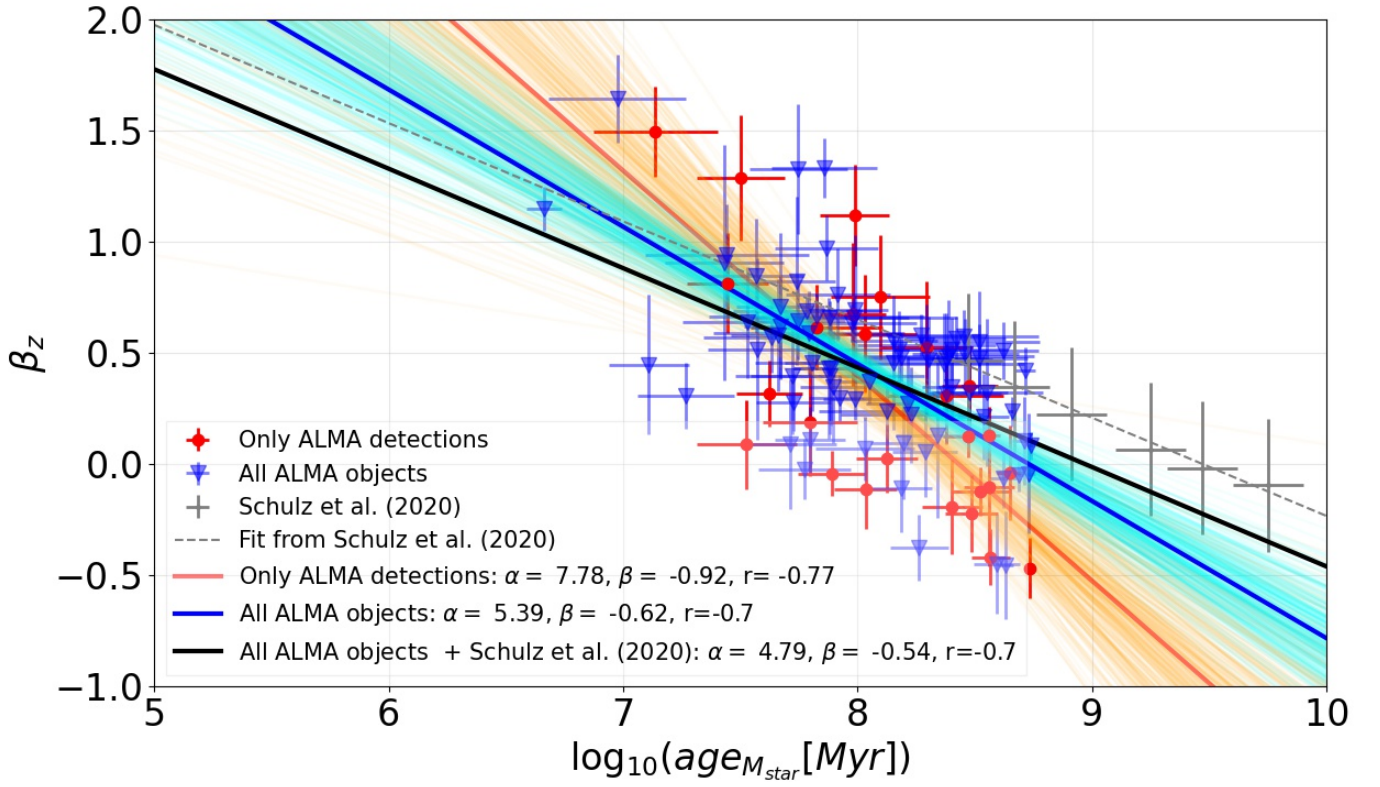


Fig. 10: Linear relation between the shift of the IRX- β_{FUV} relation at $z=0$ (namely that of Overzier et al. (2010)) vs. the mass-weighted age in years derived from the analysis of the galaxies studied here. Red symbols correspond to ALMA-detected objects, while blue objects correspond to upper limits from ALMA. We note, however, that these upper limits apply to ALMA, but not to the parameters presented in this figure: $\text{age}_{M_{star}}$ and β_z .

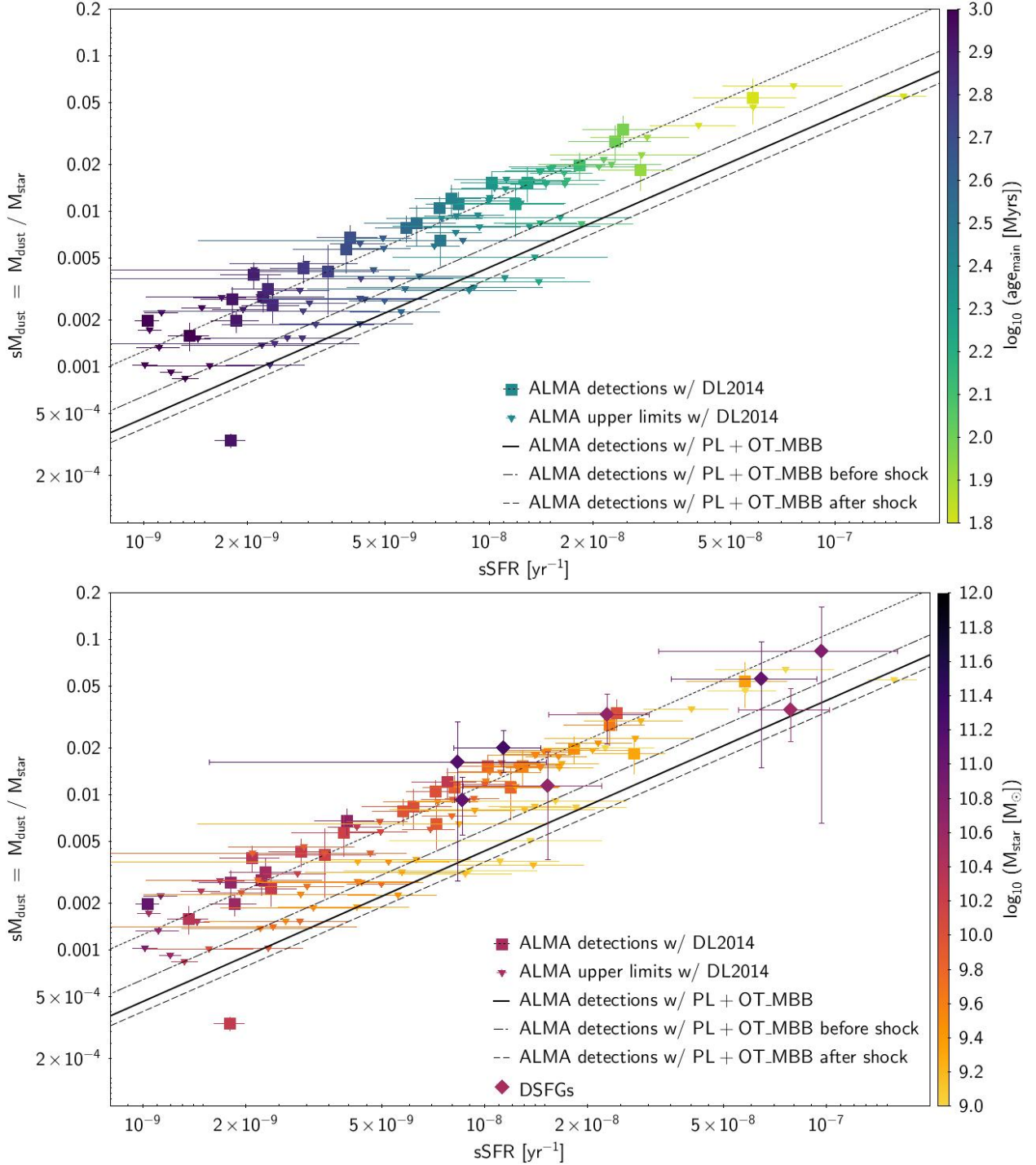


Fig. 11: Comparison of observed DFRDs with models. Top: DFRDs color-coded with $\log_{10}\text{age}_{\text{main}}$. The individual symbols were computed assuming a PL+OT_MBB emission. We clearly observe an age sequence from right to left. The lines show the trend assuming different dust emissions and different values for κ_0 . The top one assumes DL2014 dust emission. The second one from the top was derived when using an optically thin modified blackbody with $\kappa_0 = 0.637 \text{ m}^2 \text{ kg}^{-1}$ (PL+OT_MBB). We note that the factor 0.37 needed to match DL2014 to PL+OT_MBB emission was not applied. The third one from the top assumes optically thin modified blackbodies with κ_0 corresponding to SNe dust mass absorption coefficients. It corresponds to the situation before the SNe reverse shock destruction, and the bottom line represents after the reverse shock destruction. Both from Hirashita et al. (2017). Bottom: Same models as in as (a). The same objects plotted in (a) are color-coded in M_{star} . A sample of DSFGs (Tab. 8), also color-coded in M_{star} , was added to the plot with the code as follows: the upper triangle shows the maximum value, and the lower triangle shows the minimum value. These high redshift DSFGs are found on the same sequence as the other objects. However, these DSFGs have stellar masses larger than the underlying galaxy population that we study. It is important to note that the physical parameters (especially M_{star} because the IR emission is dominant) of these high redshift DSFGs have very large uncertainties and their position location in the diagram can almost cover the entire plot. Better estimates of these parameters coming from JWST would help.

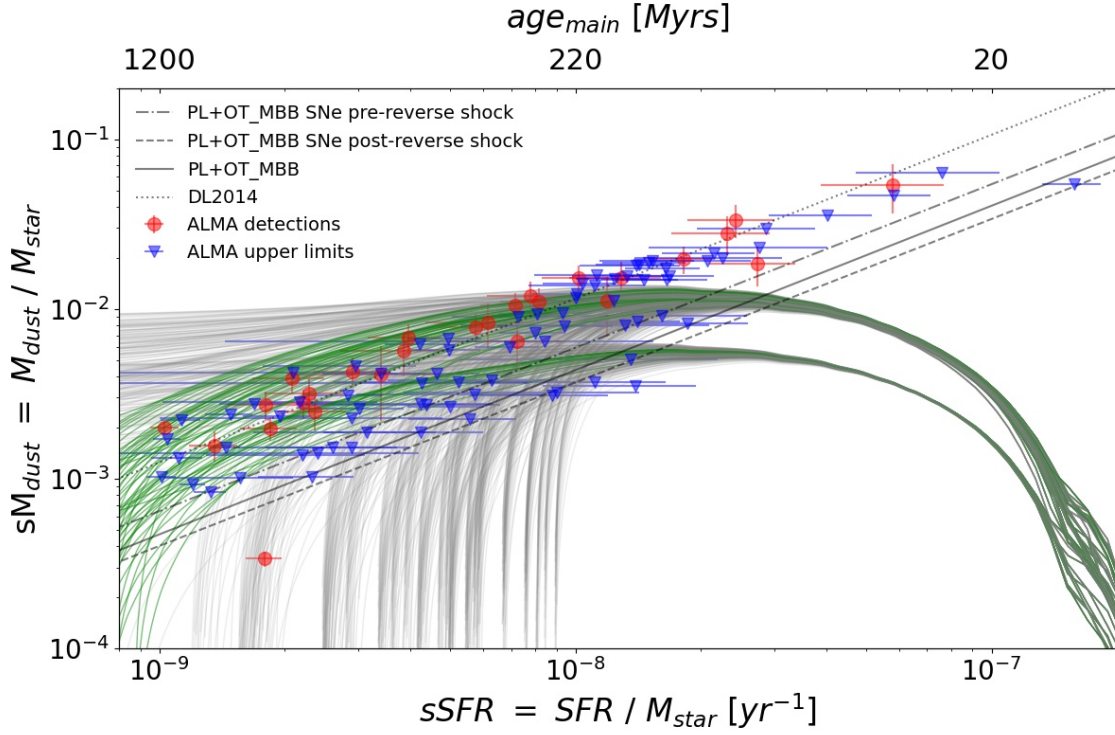


Fig. 12: DFRD for models with dust masses computed by CIGALE with DL2014 dust models. Only models with a delayed star formation history are plotted. A delayed star formation history only was consistently used in the SED fitting with CIGALE to estimate sM_{dust} and $sSFR$. The models shown do not have any grain growth in the ISM. We also show the other models in light gray to show which parameter space the models cover. On this figure, we superimposed the three lines that show the respective linear fits as in Fig. 11. The models shown are from Burgarella et al. (2020) and Nanni et al. (2020). This figure shows that most of the objects (ALMA detections and ALMA upper limits) are approximately located at the same positions as the models. Only HZ9 is found at larger $sSFR$ and sM_{dust} . If confirmed at this location in the DFRD, these objects would be very difficult to explain with these models.

Appendix A: CIGALE parameters for the initial fits

Appendix A.1: Star formation histories (SFHs)

- * A delayed SFH: $SFR(t) = t/\tau_{main}^2 \exp(-t/\tau_{main})$ with τ_{main} in the range 25 to 10000 Myrs and main ages (t or age_{main}) in the range 2 - 1200 Myrs is the first option. This type of SFH allows for SFRs to increase or decrease, depending on the age of the stellar population.
- * The second option is a delayed SFH and a final young burst with the burst age (age_{burst}) are in the range 2 to 50 Myrs, but main ages are in the range 100 to 1200 Myrs, and the fraction of burst (f_{burst}) is as follows: 0.0, 0.001, 0.01, 0.10, 0.50 and $\tau_{burst} = 20000$ Myrs, that is to say it is similar to a constant SFH given the burst ages.
- * Fixed parameters: because it was not possible to estimate τ_{main} with confidence, we also sequentially fixed and tried $\tau_{main} = 25, 250, \text{ and } 2500$ Myrs both for the delayed and burst runs before comparing the results to the above runs.

Appendix A.2: Dust characteristics

- * The models from Draine et al. (2014): because no data are available in the rest-frame near-IR and mid-IR, we could not constrain the mass fraction of PAH (q_{PAH}). However, it is generally accepted (e.g., Douglas et al. 2010; Castellano et al. 2014; Yuan et al. 2019; Bellstedt et al. 2021) that the metallicity of these galaxies are likely subsolar. Ciesla et al. (2014) show a relation between q_{PAH} and the metallicity. Without any other constraint, we arbitrarily chose a low value for the mass fraction of PAH: $q_{PAH}=0.47$. The impact of this parameter on the dust mass or luminosity is very low. We used the full range of allowed parameters for the minimum of the distribution of the starlight intensity relative to the local interstellar radiation field, U_{min} , for α , the power law slope $dU/dM = U^\alpha$, as well as for γ , the fraction of the dust heated by starlight above the lower cutoff U_{min} . For the same reason as for τ_{main} , in the SFH parameters, we also sequentially tried fixed values for $\alpha = 1.0, 2.0, \text{ and } 3.0$.
- * Modified blackbody plus a power law similar to Casey (2012): Our initial priors are the dust temperature in the range $30K \leq T_{dust} \leq 85K$ and the emissivity in the RJ part of the SED $0.5 \leq \beta_{RJ} \leq 2.0$. We kept the MIR power slope at the default $\alpha_{MIR} = 2.0$ because no data are available to constrain α_{MIR} . These values are consistent with Faisst et al. (2020), that is $40 < T_{dust}[K] < 60$ (called T_{SED} , i.e., SED dust temperature in their paper), with a median at 48 K and emissivity indices (β_d in their paper) between 1.6 and 2.4 for all galaxies, and a median of 2.0. As before, because it could not be safely estimated with the data available, we tried several fixed values for $\beta_{RJ} = 1.0, 1.5, \text{ and } 2.0$.
- * Other parameters: In addition to these parameters, we selected a Chabrier IMF and a wide range of dust attenuation. We selected CIGALE's dust attenuation law from the Calzetti and Leitherer module. It is based on the Calzetti et al. (2000) starburst attenuation curve, extended with the Leitherer et al. (2002) curve between the Lyman break and 120 nm. A nebular contribution was also added (see Boquien et al. 2019) where D_λ is the Drude profile, and the last term renormalizes the curve so that $E(B-V)$ remains equal to the input $E(B-V)$ when δ is not 0:

$$k_\lambda = k_\lambda^{starburst} \times (\lambda/\lambda_V)^\delta \times D_\lambda \frac{E(B-V)_{\delta=0}}{E(B-V)_\delta}$$

In Boquien et al. (submitted), a variation of the dust attenuation law is studied. However, changes in the shape of the dust attenuation law do not impact the IRX versus A_{FUV} relation for star forming galaxies because it is almost completely independent of the extinction mechanisms (i.e., dust and star geometry, attenuation law (e.g., Witt & Gordon 2000; Cortese et al. 2008, and references therein).

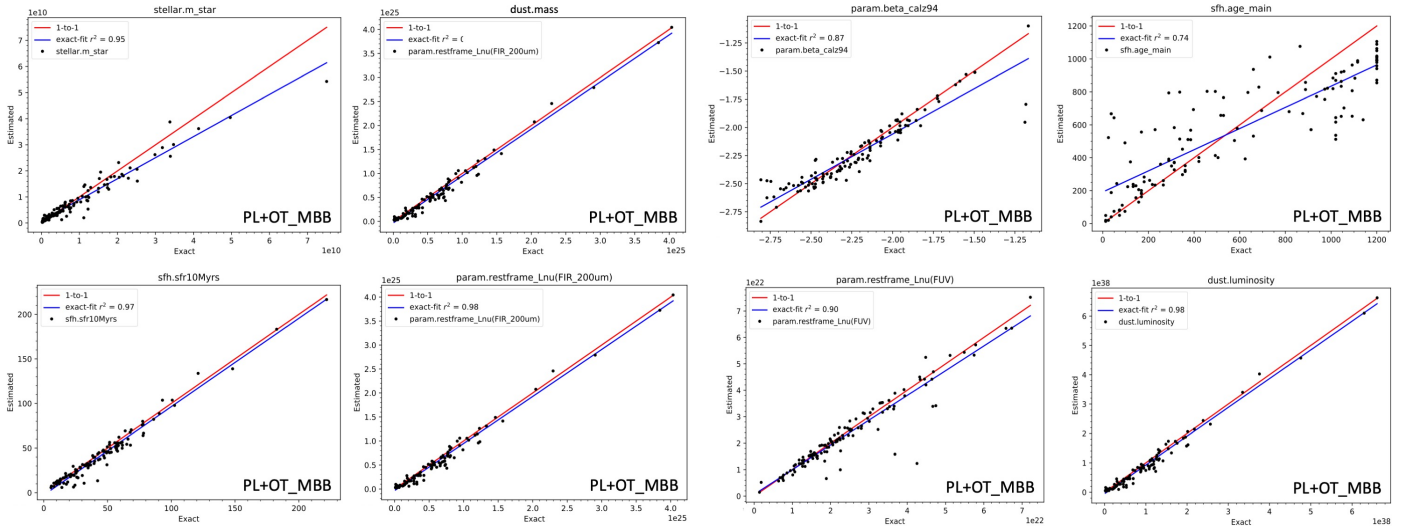
Finally, from these initial fits, we examined and discarded the fits for which the reduced $\chi^2_\nu \geq 5.0$ for each of our detected objects. These bad fits only represent a few of them with respect to all of the attempts. For each object in the sample, we computed the mean normalization factor from the CIGALE Bayesian luminosity at $200 \mu\text{m}$: $L_{200\mu\text{m}}$. After applying this normalization, all the observed SEDs started to share the same flux density at $\lambda = 200 \mu\text{m}$: $f_\nu(200 \mu\text{m}) = 1.0$ (see Fig.1) and we could then proceed to the next phase to try and combine all the observed SEDs into a single one.

Appendix B: CIGALE parameters for the final fit

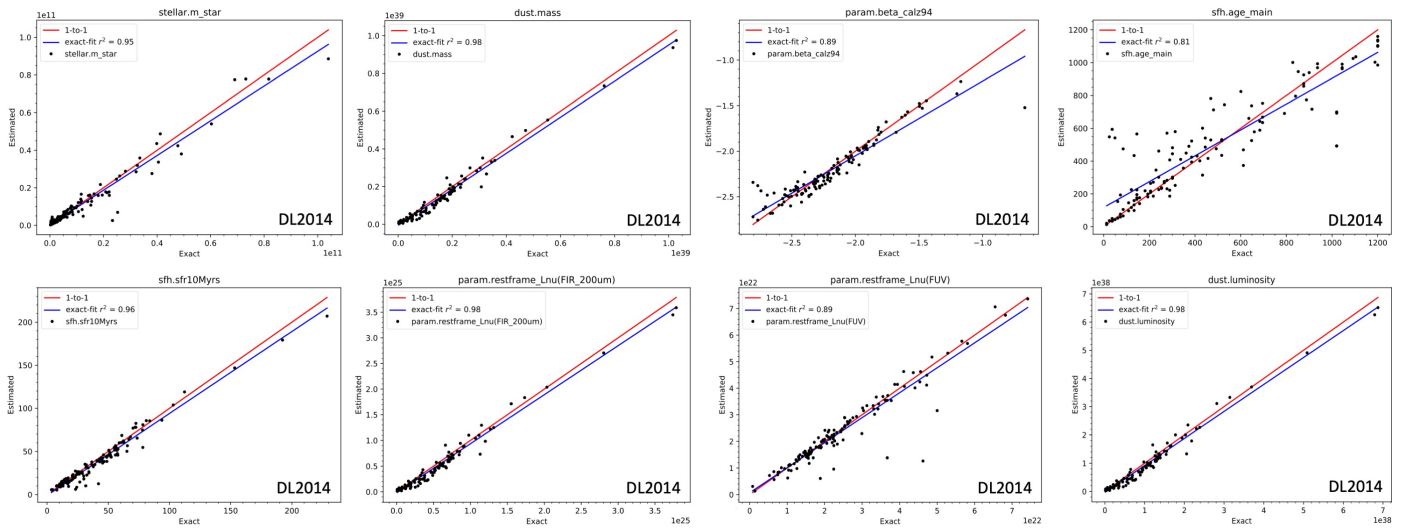
Appendix C: Results for the mock analysis performed with CIGALE

Parameters	Symbol	Range (Ph. 2, DL2014)	Range (Ph. 2, PL+OT_MBB)
Target sample		Individual Hi-z LBGs	Individual Hi-z LBGs
Delayed SFH and recent burst			
e-folding time scale of the delayed SFH	τ_{main} [Myr]	500	500
Age of the main population	Age_{main} [Myr]	101 log values in [2 - 1200]	101 log values in [2 - 1200]
Burst	f_{burst}	No burst	No burst
SSP			
SSP		BC03	BC03
Initial mass function	IMF	Chabrier	Chabrier
Metallicity	Z	0.004	0.004
Nebular emission			
Ionization parameter	$\log U$	-2.5, -2.0, -1.5	-2.5, -2.0, -1.5
Line width [km/s]	—	100	100
Dust attenuation law			
Color excess for both the old and young stellar populations	E_{BV_lines}	101 log values in [0.01, 1.0]	101 log values in [0.01, 1.0]
Bump amplitude	$uv_bump_amplitude$	0.0	0.0
Power law slope	$power\ law_slope$	0.0	0.0
Dust emission (DL2014)			
Mass fraction of PAH	q_{PAH}	0.47	—
Minimum radiation field	U_{min}	17.0	—
Power law slope $dU/dM \approx U^\alpha$	— α	2.4	—
Dust fraction in PDRs	γ	0.54	—
Dust emission (PL + OT_MBB)			
Dust temperature	T_{dust}	—	54.1
Emissivity	β_{RJ}	—	0.87
Slope of the MIR power law	α_{MIR}	—	2.0
No AGN emission			

Table B.1: CIGALE modules and input parameters used for all the fits. BC03 means Bruzual & Charlot (2003), and the Chabrier IMF refers to Chabrier (2003).



(a) Mock analysis using the power law and OT_MBB in the mid-IR as in Casey et al. (2012) for the IR template.



(b) Mock analysis using the DL2014 model for the IR template.

Fig. C.1: Results from the mock analysis performed with CIGALE where we compared input parameters (i.e., parameters from the best fit for each object) to the same parameters estimated by CIGALE with the very same priors used for the true analysis (see Boquien et al. 2019). We note that some parameters were estimated from another one via a linear relation, e.g., M_{dust} from $L_{200\mu m}$, which explains why the figures are identical.

Appendix D: The observed IR composite templateTable D.1: IR template for each of the models, normalized to $200 \mu\text{m}$. Only the first rows are given here.

Beginning of table			
$\lambda[\mu\text{m}]$	$F_{\nu}(\text{DL2014})$	$F_{\nu}(\text{PL+OTMBB})$	$F_{\nu}(\text{PL+GMBB})$
20.000	0.181	0.033	0.228
20.140	0.186	0.036	0.233
20.320	0.192	0.039	0.239
20.510	0.198	0.042	0.246
20.700	0.205	0.046	0.253
20.867	0.212	0.049	0.259
20.890	0.213	0.049	0.260
21.090	0.220	0.054	0.267
21.280	0.228	0.058	0.275
21.480	0.236	0.063	0.283
21.680	0.244	0.068	0.291
21.880	0.253	0.073	0.300

Continuation of Table D.1			
$\lambda[\mu\text{m}]$	$F_{\nu}(\text{DL2014})$	$F_{\nu}(\text{PL+OTMBB})$	$F_{\nu}(\text{PL+GMBB})$
22.080	0.262	0.079	0.309
22.082	0.262	0.079	0.309
22.280	0.271	0.085	0.318
22.490	0.281	0.091	0.328
22.700	0.291	0.098	0.338
22.910	0.301	0.105	0.348
23.120	0.312	0.113	0.359
23.330	0.323	0.121	0.370
23.367	0.325	0.123	0.372
23.550	0.334	0.130	0.382
23.770	0.346	0.139	0.394
23.990	0.358	0.149	0.406
24.210	0.370	0.159	0.419
24.430	0.383	0.169	0.432
24.660	0.396	0.180	0.446
24.728	0.400	0.184	0.450
24.890	0.410	0.192	0.460
25.120	0.424	0.205	0.474
25.350	0.438	0.217	0.489
25.590	0.453	0.231	0.505
25.820	0.468	0.245	0.521
26.060	0.484	0.260	0.537
26.167	0.491	0.267	0.545
26.300	0.500	0.275	0.554
26.550	0.516	0.292	0.572
26.790	0.533	0.308	0.590
27.040	0.550	0.326	0.608
27.290	0.568	0.344	0.627
27.540	0.586	0.363	0.647
27.690	0.596	0.374	0.658
27.800	0.604	0.383	0.667
28.050	0.623	0.403	0.687
28.310	0.642	0.424	0.708
28.580	0.662	0.447	0.730
28.840	0.682	0.469	0.752
29.110	0.703	0.493	0.774
29.302	0.718	0.510	0.791
29.380	0.724	0.517	0.798
29.650	0.745	0.542	0.821
29.920	0.767	0.567	0.845
30.200	0.789	0.594	0.869
30.480	0.812	0.622	0.894
30.760	0.835	0.650	0.920
31.008	0.855	0.675	0.942
31.050	0.858	0.679	0.946
31.330	0.882	0.708	0.972
31.620	0.907	0.739	0.999
31.920	0.931	0.771	1.027
32.210	0.956	0.802	1.054
32.510	0.982	0.835	1.082
32.810	1.007	0.869	1.111
32.813	1.008	0.869	1.111
33.110	1.034	0.902	1.140
33.370	1.056	0.932	1.165
33.395	1.058	0.935	1.167
33.420	1.063	0.940	1.172
33.420	1.063	0.940	1.172
33.420	1.065	0.942	1.175
33.445	1.311	1.175	1.446
33.470	2.250	2.060	2.483
33.495	1.317	1.182	1.452
33.520	1.072	0.951	1.182

Continuation of Table D.1			
$\lambda[\mu\text{m}]$	$F_{\nu}(\text{DL2014})$	$F_{\nu}(\text{PL+OTMBB})$	$F_{\nu}(\text{PL+GMBB})$
33.545	1.072	0.952	1.181
33.570	1.074	0.955	1.184
33.730	1.088	0.974	1.199
34.040	1.116	1.010	1.229
34.360	1.144	1.047	1.260
34.670	1.172	1.084	1.290
34.705	1.175	1.088	1.294
34.724	1.176	1.090	1.296
34.732	1.177	1.091	1.296
34.758	1.180	1.094	1.299
34.784	1.190	1.105	1.310
34.810	1.221	1.136	1.345
34.836	1.194	1.111	1.315
34.862	1.189	1.107	1.309
34.862	1.189	1.107	1.309
34.888	1.191	1.110	1.311
34.888	1.191	1.110	1.311
34.915	1.194	1.113	1.314
34.990	1.201	1.122	1.321
35.320	1.230	1.162	1.353
35.650	1.259	1.202	1.385
35.902	1.283	1.232	1.410
35.929	1.285	1.235	1.412
35.956	1.288	1.239	1.415
35.970	1.300	1.250	1.428
35.983	1.311	1.261	1.440
36.010	1.390	1.337	1.527
36.037	1.316	1.268	1.445
36.064	1.298	1.252	1.426
36.064	1.298	1.252	1.426
36.091	1.300	1.255	1.428
36.118	1.303	1.258	1.431
36.310	1.320	1.282	1.449
36.640	1.350	1.322	1.481
36.745	1.359	1.335	1.491
36.980	1.381	1.364	1.514
37.330	1.412	1.407	1.548
37.670	1.444	1.449	1.580
38.020	1.476	1.492	1.613
38.370	1.507	1.534	1.646
38.730	1.540	1.579	1.680
38.884	1.554	1.597	1.695
39.080	1.572	1.621	1.713
39.450	1.605	1.666	1.747
39.810	1.637	1.710	1.780
40.000	1.654	1.733	1.798
40.180	1.670	1.755	1.814
40.550	1.704	1.799	1.848
40.930	1.736	1.845	1.882
41.148	1.756	1.870	1.901
41.300	1.770	1.888	1.914
41.690	1.804	1.934	1.948
42.070	1.838	1.978	1.981
42.460	1.871	2.023	2.015
42.850	1.906	2.068	2.047
43.250	1.940	2.113	2.081
43.543	1.965	2.145	2.105
43.650	1.974	2.157	2.113
44.060	2.008	2.202	2.146
44.460	2.042	2.246	2.178
44.870	2.076	2.289	2.210
45.290	2.111	2.333	2.242

Continuation of Table D.1			
$\lambda[\mu\text{m}]$	$F_{\nu}(\text{DL2014})$	$F_{\nu}(\text{PL+OTMBB})$	$F_{\nu}(\text{PL+GMBB})$
45.710	2.145	2.377	2.274
46.078	2.175	2.414	2.301
46.130	2.179	2.419	2.305
46.560	2.213	2.462	2.336
46.990	2.247	2.504	2.366
47.420	2.280	2.545	2.396
47.860	2.315	2.586	2.426
48.310	2.348	2.627	2.456
48.750	2.381	2.666	2.484
48.761	2.382	2.667	2.485
49.200	2.414	2.705	2.513
49.660	2.447	2.744	2.541
50.120	2.480	2.782	2.569
50.580	2.513	2.819	2.596
51.050	2.544	2.855	2.622
51.520	2.576	2.891	2.648
51.599	2.581	2.896	2.653
51.644	2.584	2.900	2.655
51.683	2.587	2.903	2.657
51.683	2.587	2.903	2.657
51.722	2.598	2.914	2.669
51.722	2.598	2.914	2.669
51.761	3.551	3.812	3.720
51.761	3.551	3.812	3.720
51.800	7.162	7.216	7.707
51.839	3.559	3.820	3.727
51.878	2.608	2.925	2.677
51.917	2.602	2.920	2.670
51.956	2.604	2.922	2.672
51.956	2.604	2.922	2.672
52.000	2.607	2.926	2.674
52.480	2.638	2.959	2.699
52.970	2.669	2.993	2.724
53.460	2.698	3.025	2.748
53.950	2.728	3.056	2.771
54.450	2.757	3.086	2.794
54.603	2.765	3.095	2.800
54.950	2.785	3.116	2.816
55.460	2.813	3.144	2.837
55.980	2.839	3.172	2.858
56.490	2.866	3.198	2.878
57.020	2.892	3.224	2.898
57.038	2.893	3.225	2.899
57.081	2.895	3.227	2.901
57.081	2.895	3.227	2.901
57.124	2.898	3.229	2.903
57.124	2.898	3.229	2.903
57.167	2.989	3.315	3.002
57.210	3.326	3.633	3.374
57.253	2.993	3.319	3.005
57.253	2.993	3.319	3.005
57.296	2.906	3.237	2.909
57.339	2.908	3.239	2.910
57.382	2.910	3.241	2.911
57.382	2.910	3.241	2.911
57.540	2.917	3.248	2.917
57.782	2.928	3.259	2.925
58.080	2.942	3.271	2.936
58.610	2.966	3.293	2.953
59.160	2.989	3.315	2.970
59.700	3.011	3.335	2.987
60.000	3.023	3.345	2.995

Continuation of Table D.1			
$\lambda[\mu\text{m}]$	$F_{\nu}(\text{DL2014})$	$F_{\nu}(\text{PL+OTMBB})$	$F_{\nu}(\text{PL+GMBB})$
60.260	3.033	3.354	3.002
60.810	3.054	3.372	3.017
61.145	3.066	3.382	3.026
61.380	3.074	3.389	3.032
61.940	3.093	3.404	3.045
62.520	3.112	3.419	3.058
62.980	3.125	3.430	3.068
62.980	3.125	3.430	3.068
63.028	3.126	3.431	3.069
63.028	3.126	3.431	3.069
63.075	3.128	3.432	3.070
63.100	3.131	3.434	3.073
63.123	3.133	3.437	3.075
63.170	3.149	3.452	3.092
63.217	3.136	3.439	3.077
63.265	3.133	3.436	3.074
63.265	3.133	3.436	3.074
63.312	3.135	3.437	3.075
63.360	3.136	3.438	3.076
63.680	3.146	3.445	3.082
64.270	3.161	3.456	3.093
64.705	3.173	3.463	3.100
64.860	3.177	3.466	3.103
65.460	3.191	3.475	3.112
66.070	3.204	3.483	3.121
66.680	3.216	3.490	3.129
67.300	3.227	3.495	3.136
67.920	3.238	3.500	3.142
68.472	3.245	3.503	3.147
68.550	3.246	3.503	3.148
69.180	3.256	3.506	3.153
69.820	3.263	3.507	3.157
70.470	3.269	3.508	3.161
71.120	3.275	3.507	3.163
71.780	3.279	3.505	3.165
72.440	3.284	3.502	3.167
72.458	3.284	3.502	3.167
73.110	3.286	3.498	3.167
73.790	3.287	3.493	3.167
74.470	3.289	3.488	3.167
75.160	3.288	3.481	3.165
75.860	3.287	3.473	3.163
76.560	3.284	3.465	3.160
76.676	3.284	3.463	3.159
77.270	3.281	3.455	3.156
77.980	3.277	3.445	3.152
78.700	3.272	3.433	3.147
79.430	3.266	3.421	3.141
80.000	3.262	3.411	3.136
80.170	3.260	3.408	3.134
80.910	3.251	3.394	3.127
81.140	3.249	3.390	3.125
81.660	3.243	3.380	3.119
82.410	3.234	3.364	3.111
83.180	3.224	3.348	3.101
83.950	3.213	3.331	3.091
84.720	3.201	3.314	3.081
85.510	3.188	3.295	3.070
85.863	3.182	3.287	3.064
86.300	3.175	3.276	3.058
87.100	3.160	3.257	3.045
87.900	3.145	3.237	3.032

Continuation of Table D.1			
$\lambda[\mu\text{m}]$	$F_{\nu}(\text{DL2014})$	$F_{\nu}(\text{PL+OTMBB})$	$F_{\nu}(\text{PL+GMBB})$
88.065	3.143	3.232	3.030
88.065	3.143	3.232	3.030
88.131	3.141	3.231	3.029
88.197	3.158	3.246	3.047
88.197	3.158	3.246	3.047
88.264	5.067	5.045	5.156
88.264	5.067	5.045	5.156
88.330	12.325	11.885	13.169
88.396	5.071	5.047	5.160
88.463	3.153	3.239	3.043
88.529	3.134	3.220	3.022
88.595	3.133	3.219	3.021
88.720	3.130	3.215	3.019
89.540	3.114	3.194	3.004
90.360	3.098	3.172	2.990
90.862	3.087	3.159	2.980
91.200	3.080	3.150	2.974
92.040	3.062	3.127	2.958
92.900	3.043	3.103	2.941
93.760	3.024	3.079	2.924
94.620	3.004	3.054	2.907
95.500	2.983	3.029	2.888
96.151	2.968	3.011	2.875
96.380	2.962	3.004	2.870
97.270	2.940	2.978	2.850
98.170	2.919	2.952	2.831
99.080	2.896	2.926	2.811
100.000	2.872	2.899	2.790
100.900	2.848	2.873	2.770
100.926	2.848	2.872	2.769
101.749	2.828	2.848	2.750
101.861	2.825	2.844	2.748
101.900	2.824	2.843	2.747
102.800	2.799	2.817	2.726
102.804	2.799	2.816	2.726
103.757	2.776	2.789	2.703
103.800	2.775	2.787	2.702
104.700	2.750	2.761	2.681
104.718	2.750	2.760	2.681
105.688	2.725	2.732	2.658
105.700	2.725	2.732	2.657
106.666	2.701	2.703	2.634
106.700	2.700	2.702	2.633
107.600	2.674	2.676	2.612
107.654	2.673	2.675	2.611
107.672	2.672	2.674	2.610
108.600	2.648	2.647	2.588
108.652	2.647	2.646	2.586
109.600	2.622	2.618	2.564
109.658	2.621	2.617	2.562
110.674	2.597	2.587	2.538
110.700	2.596	2.587	2.537
111.699	2.570	2.558	2.513
111.700	2.570	2.558	2.513
112.700	2.543	2.530	2.488
112.733	2.543	2.529	2.488
113.777	2.518	2.499	2.462
113.800	2.518	2.498	2.462
113.940	2.514	2.494	2.458
114.800	2.491	2.470	2.437
114.831	2.491	2.469	2.436
115.895	2.466	2.440	2.411

Continuation of Table D.1			
$\lambda[\mu\text{m}]$	$F_{\nu}(\text{DL2014})$	$F_{\nu}(\text{PL+OTMBB})$	$F_{\nu}(\text{PL+GMBB})$
115.900	2.466	2.440	2.411
116.900	2.440	2.412	2.386
116.968	2.438	2.410	2.385
118.000	2.414	2.382	2.360
118.052	2.413	2.380	2.358
119.100	2.389	2.352	2.333
119.145	2.388	2.351	2.332
120.000	2.368	2.328	2.312
120.200	2.363	2.323	2.307
120.249	2.362	2.321	2.306
120.573	2.355	2.312	2.298
121.300	2.339	2.293	2.280
121.335	2.338	2.292	2.280
121.362	2.338	2.291	2.279
121.426	2.337	2.290	2.277
121.426	2.337	2.290	2.277
121.517	2.335	2.287	2.275
121.609	2.335	2.287	2.276
121.700	2.342	2.293	2.283
121.791	2.332	2.283	2.271
121.791	2.332	2.283	2.271
121.883	2.327	2.278	2.267
121.883	2.327	2.278	2.267
121.974	2.325	2.275	2.265
122.065	2.323	2.273	2.262
122.486	2.315	2.262	2.252
122.500	2.314	2.262	2.252
123.600	2.289	2.233	2.226
123.621	2.289	2.232	2.225
124.700	2.265	2.205	2.200
124.766	2.264	2.203	2.198
125.900	2.242	2.174	2.172
125.922	2.241	2.173	2.172
127.088	2.219	2.144	2.144
127.100	2.219	2.144	2.144
127.592	2.209	2.132	2.133
128.200	2.197	2.116	2.119
128.265	2.195	2.115	2.117
129.400	2.175	2.087	2.091
129.453	2.174	2.086	2.090
130.600	2.154	2.058	2.064
130.652	2.153	2.057	2.063
131.800	2.132	2.029	2.037
131.862	2.131	2.028	2.036
133.000	2.110	2.001	2.010
133.083	2.109	1.999	2.008
134.300	2.089	1.971	1.982
134.316	2.088	1.970	1.981
135.020	2.075	1.954	1.966
135.500	2.066	1.943	1.955
135.560	2.065	1.942	1.954
136.800	2.042	1.914	1.927
136.816	2.042	1.914	1.927
138.000	2.016	1.887	1.902
138.083	2.014	1.885	1.900
139.300	1.987	1.859	1.874
139.362	1.986	1.857	1.873
140.000	1.971	1.844	1.859
140.600	1.956	1.831	1.847
140.653	1.955	1.830	1.846
141.900	1.923	1.803	1.820
141.955	1.921	1.802	1.819

Continuation of Table D.1			
$\lambda[\mu\text{m}]$	$F_{\nu}(\text{DL2014})$	$F_{\nu}(\text{PL+OTMBB})$	$F_{\nu}(\text{PL+GMBB})$
142.880	1.897	1.783	1.800
143.200	1.888	1.776	1.794
143.270	1.886	1.775	1.792
144.500	1.851	1.749	1.767
144.597	1.849	1.747	1.765
145.063	1.837	1.738	1.756
145.172	1.834	1.736	1.754
145.282	1.831	1.733	1.752
145.282	1.831	1.733	1.752
145.391	1.829	1.732	1.751
145.500	1.830	1.733	1.752
145.609	1.824	1.728	1.746
145.718	1.820	1.725	1.743
145.828	1.817	1.723	1.741
145.900	1.815	1.721	1.740
145.937	1.814	1.720	1.739
145.937	1.814	1.720	1.739
147.200	1.778	1.695	1.714
147.288	1.776	1.694	1.712
148.600	1.742	1.668	1.687
148.652	1.741	1.667	1.686
150.000	1.706	1.641	1.660
150.029	1.705	1.641	1.660
151.198	1.676	1.619	1.638
151.400	1.671	1.615	1.634
151.419	1.671	1.615	1.634
152.800	1.636	1.589	1.608
152.821	1.636	1.589	1.608
154.200	1.603	1.564	1.583
154.237	1.602	1.563	1.582
155.600	1.570	1.539	1.558
155.665	1.569	1.538	1.557
157.000	1.538	1.514	1.533
157.107	1.536	1.513	1.531
157.127	1.535	1.512	1.531
157.245	1.533	1.510	1.529
157.363	1.531	1.508	1.527
157.482	1.556	1.533	1.556
157.600	1.660	1.631	1.671
157.718	1.551	1.529	1.552
157.837	1.521	1.500	1.519
157.955	1.518	1.498	1.516
158.073	1.516	1.496	1.514
158.500	1.506	1.489	1.507
158.562	1.505	1.488	1.506
160.000	1.475	1.463	1.481
160.031	1.474	1.463	1.481
161.400	1.445	1.440	1.458
161.513	1.443	1.439	1.456
162.900	1.415	1.416	1.433
163.009	1.413	1.415	1.432
164.400	1.386	1.392	1.409
164.519	1.384	1.391	1.407
165.959	1.358	1.368	1.384
166.000	1.358	1.368	1.384
166.043	1.357	1.367	1.383
167.500	1.329	1.345	1.360
167.581	1.328	1.344	1.359
169.000	1.302	1.323	1.337
169.133	1.300	1.321	1.335
169.824	1.288	1.311	1.325
170.600	1.275	1.299	1.313

Continuation of Table D.1			
$\lambda[\mu\text{m}]$	$F_{\nu}(\text{DL2014})$	$F_{\nu}(\text{PL+OTMBB})$	$F_{\nu}(\text{PL+GMBB})$
170.699	1.273	1.298	1.312
172.200	1.248	1.276	1.290
172.281	1.246	1.275	1.288
173.780	1.222	1.254	1.267
173.800	1.221	1.254	1.266
173.876	1.220	1.253	1.265
175.400	1.196	1.232	1.244
175.487	1.194	1.231	1.242
177.000	1.170	1.211	1.221
177.112	1.169	1.209	1.220
177.828	1.158	1.200	1.210
178.600	1.146	1.190	1.200
178.753	1.143	1.188	1.197
180.300	1.121	1.168	1.177
180.408	1.120	1.167	1.175
181.970	1.097	1.147	1.155
182.000	1.097	1.147	1.155
182.079	1.096	1.146	1.154
183.700	1.073	1.126	1.133
183.766	1.072	1.125	1.132
185.400	1.050	1.106	1.112
185.468	1.049	1.105	1.111
186.209	1.039	1.096	1.102
187.100	1.027	1.086	1.091
187.186	1.026	1.085	1.090
188.800	1.004	1.066	1.070
188.919	1.003	1.065	1.069
190.500	0.982	1.047	1.050
190.546	0.982	1.047	1.050
190.669	0.980	1.045	1.048
192.300	0.961	1.027	1.030
192.435	0.959	1.026	1.028
194.100	0.939	1.008	1.009
194.217	0.938	1.007	1.008
194.984	0.929	0.999	1.000
195.900	0.918	0.989	0.990
196.016	0.917	0.988	0.988
197.700	0.897	0.971	0.970
197.832	0.896	0.970	0.969
199.500	0.877	0.953	0.951
199.526	0.877	0.953	0.951
199.664	0.875	0.952	0.949
201.400	0.857	0.935	0.932
201.514	0.856	0.934	0.931
203.200	0.838	0.918	0.914
203.380	0.836	0.916	0.912
204.174	0.828	0.909	0.904
204.783	0.822	0.903	0.898
204.938	0.820	0.902	0.897
204.938	0.820	0.902	0.897
205.092	0.818	0.900	0.895
205.092	0.818	0.900	0.895
205.100	0.818	0.900	0.895
205.246	0.819	0.900	0.895
205.246	0.819	0.900	0.895
205.264	0.819	0.901	0.896
205.400	0.823	0.905	0.901
205.554	0.816	0.898	0.893
205.708	0.812	0.895	0.889
205.862	0.811	0.893	0.888
206.017	0.809	0.892	0.886
206.017	0.809	0.892	0.886

Continuation of Table D.1			
$\lambda[\mu\text{m}]$	$F_{\nu}(\text{DL2014})$	$F_{\nu}(\text{PL+OTMBB})$	$F_{\nu}(\text{PL+GMBB})$
207.000	0.799	0.883	0.877
207.165	0.798	0.882	0.875
208.900	0.781	0.866	0.859
208.930	0.780	0.866	0.859
209.084	0.779	0.865	0.858
210.900	0.763	0.849	0.841
211.020	0.761	0.848	0.840
212.800	0.745	0.833	0.824
212.975	0.743	0.832	0.823
213.796	0.736	0.825	0.815
214.800	0.727	0.817	0.807
214.947	0.726	0.816	0.805
216.800	0.710	0.801	0.790
216.938	0.709	0.800	0.789
218.776	0.693	0.785	0.774
218.800	0.693	0.785	0.773
218.948	0.692	0.784	0.772
220.800	0.676	0.770	0.757
220.976	0.675	0.769	0.756
222.800	0.660	0.755	0.742
223.022	0.658	0.754	0.740
223.872	0.652	0.748	0.733
224.900	0.644	0.740	0.725
225.088	0.643	0.739	0.724
227.000	0.629	0.725	0.710
227.173	0.627	0.724	0.709
229.087	0.613	0.711	0.695
229.100	0.613	0.711	0.695
229.277	0.612	0.710	0.693
231.200	0.598	0.697	0.680
231.401	0.597	0.696	0.678
233.300	0.583	0.683	0.665
233.544	0.582	0.682	0.664
234.423	0.576	0.676	0.658
235.500	0.569	0.669	0.651
235.707	0.568	0.668	0.649
237.700	0.555	0.656	0.636
237.890	0.554	0.655	0.635
239.883	0.541	0.643	0.622
239.900	0.541	0.643	0.622
240.093	0.540	0.642	0.621
242.100	0.528	0.630	0.609
242.317	0.526	0.628	0.607
244.300	0.514	0.617	0.595
244.562	0.513	0.616	0.594
245.471	0.507	0.611	0.588
246.600	0.501	0.605	0.582
246.827	0.500	0.603	0.581
248.900	0.488	0.592	0.569
249.113	0.487	0.591	0.567
251.189	0.475	0.580	0.556
251.200	0.475	0.580	0.556
251.420	0.473	0.579	0.555
253.500	0.462	0.568	0.544
253.749	0.460	0.567	0.542
255.900	0.449	0.556	0.531
256.099	0.448	0.555	0.530
257.040	0.443	0.551	0.525
258.200	0.437	0.545	0.519
258.471	0.435	0.544	0.518
260.600	0.424	0.534	0.507
260.865	0.423	0.533	0.506

Continuation of Table D.1			
$\lambda[\mu\text{m}]$	$F_{\nu}(\text{DL2014})$	$F_{\nu}(\text{PL+OTMBB})$	$F_{\nu}(\text{PL+GMBB})$
263.000	0.413	0.523	0.496
263.027	0.412	0.523	0.496
263.282	0.411	0.521	0.494
265.500	0.401	0.512	0.484
265.720	0.400	0.511	0.483
267.900	0.390	0.501	0.473
268.181	0.389	0.500	0.472
269.153	0.384	0.496	0.468
270.400	0.379	0.491	0.462
270.665	0.378	0.490	0.461
272.900	0.368	0.480	0.451
273.172	0.367	0.479	0.450
275.400	0.358	0.470	0.441
275.423	0.358	0.470	0.441
275.702	0.357	0.469	0.440
278.000	0.348	0.460	0.430
278.256	0.347	0.459	0.429
280.500	0.338	0.451	0.421
280.833	0.337	0.450	0.419
281.838	0.333	0.446	0.415
283.100	0.328	0.441	0.411
283.434	0.327	0.440	0.409
285.800	0.319	0.432	0.401
286.060	0.318	0.431	0.400
288.400	0.310	0.423	0.391
288.403	0.310	0.423	0.391
288.709	0.309	0.422	0.390
291.100	0.301	0.414	0.382
291.383	0.300	0.413	0.381
293.800	0.293	0.405	0.373
294.082	0.292	0.404	0.372
295.121	0.289	0.401	0.368
296.500	0.284	0.396	0.364
296.806	0.283	0.395	0.363
299.200	0.276	0.388	0.355
299.555	0.275	0.387	0.354
301.995	0.268	0.379	0.347
302.000	0.268	0.379	0.347
302.329	0.267	0.378	0.346
304.800	0.261	0.371	0.338
305.130	0.260	0.370	0.337
307.600	0.253	0.363	0.330
307.956	0.252	0.362	0.329
309.030	0.250	0.359	0.326
310.500	0.246	0.355	0.322
310.808	0.245	0.354	0.321
313.300	0.239	0.348	0.314
313.687	0.238	0.347	0.313
316.200	0.232	0.340	0.307
316.228	0.232	0.340	0.306
316.592	0.231	0.339	0.306
319.200	0.225	0.333	0.299
319.525	0.225	0.332	0.298
322.100	0.219	0.325	0.292
322.484	0.218	0.325	0.291
323.594	0.216	0.322	0.288
325.100	0.212	0.318	0.284
325.471	0.212	0.317	0.283
328.100	0.206	0.311	0.277
328.486	0.206	0.310	0.276
331.100	0.200	0.305	0.271
331.131	0.200	0.305	0.270

Continuation of Table D.1			
$\lambda[\mu\text{m}]$	$F_{\nu}(\text{DL2014})$	$F_{\nu}(\text{PL+OTMBB})$	$F_{\nu}(\text{PL+GMBB})$
331.528	0.200	0.304	0.270
334.200	0.194	0.298	0.264
334.599	0.194	0.297	0.263
337.300	0.189	0.291	0.257
337.698	0.188	0.290	0.256
338.844	0.186	0.288	0.254
340.400	0.183	0.285	0.251
340.826	0.183	0.284	0.250
343.600	0.178	0.279	0.244
343.983	0.177	0.278	0.244
346.700	0.173	0.273	0.238
346.737	0.173	0.272	0.238
347.169	0.172	0.272	0.237
349.900	0.168	0.267	0.232
350.384	0.167	0.266	0.232
353.200	0.163	0.261	0.226
353.630	0.162	0.260	0.226
354.813	0.161	0.258	0.224
356.500	0.158	0.255	0.221
356.905	0.158	0.254	0.220
359.700	0.153	0.249	0.215
360.211	0.153	0.248	0.214
363.078	0.149	0.244	0.210
363.100	0.149	0.244	0.210
363.547	0.148	0.243	0.209
366.400	0.145	0.238	0.204
366.914	0.144	0.237	0.204
369.800	0.140	0.233	0.199
370.313	0.140	0.232	0.198
371.535	0.138	0.230	0.197
373.300	0.136	0.227	0.194
373.743	0.136	0.227	0.193
376.700	0.132	0.222	0.189
377.204	0.132	0.222	0.188
380.189	0.128	0.217	0.184
380.200	0.128	0.217	0.184
380.698	0.128	0.217	0.183
383.700	0.125	0.213	0.179
384.224	0.124	0.212	0.179
387.300	0.121	0.208	0.175
387.783	0.120	0.207	0.174
389.045	0.119	0.205	0.173
390.800	0.117	0.203	0.170
391.375	0.117	0.202	0.170
394.500	0.114	0.198	0.166
395.000	0.114	0.198	0.165
398.100	0.111	0.194	0.162
398.107	0.111	0.194	0.162
398.658	0.110	0.193	0.161
401.800	0.107	0.190	0.157
402.351	0.107	0.189	0.157
405.500	0.104	0.185	0.153
406.077	0.104	0.185	0.153
407.380	0.103	0.183	0.151
409.300	0.101	0.181	0.149
409.838	0.101	0.180	0.149
413.000	0.098	0.177	0.145
413.634	0.098	0.176	0.145
416.869	0.095	0.173	0.142
416.900	0.095	0.173	0.142
417.466	0.095	0.172	0.141
420.700	0.092	0.169	0.138

Continuation of Table D.1			
$\lambda[\mu\text{m}]$	$F_{\nu}(\text{DL2014})$	$F_{\nu}(\text{PL+OTMBB})$	$F_{\nu}(\text{PL+GMBB})$
421.332	0.092	0.168	0.137
424.600	0.090	0.165	0.134
425.235	0.089	0.165	0.134
426.580	0.088	0.163	0.132
428.500	0.087	0.161	0.131
429.173	0.087	0.161	0.130
432.500	0.085	0.158	0.127
433.148	0.084	0.157	0.127
436.500	0.082	0.154	0.124
436.516	0.082	0.154	0.124
437.160	0.082	0.154	0.123
440.600	0.080	0.151	0.121
441.209	0.079	0.150	0.120
444.600	0.077	0.147	0.117
445.296	0.077	0.147	0.117
446.684	0.076	0.145	0.116
448.700	0.075	0.144	0.114
449.420	0.075	0.143	0.114
452.900	0.073	0.140	0.111
453.583	0.072	0.140	0.111
457.088	0.071	0.137	0.108
457.100	0.071	0.137	0.108
457.784	0.070	0.137	0.108
461.300	0.069	0.134	0.105
462.024	0.068	0.133	0.105
465.600	0.067	0.131	0.103
466.303	0.066	0.130	0.102
467.735	0.066	0.129	0.101
469.900	0.065	0.128	0.100
470.622	0.064	0.127	0.099
474.200	0.063	0.125	0.097
474.981	0.062	0.124	0.097
478.600	0.061	0.122	0.095
478.630	0.061	0.122	0.095
479.381	0.061	0.122	0.094
483.100	0.059	0.119	0.092
483.821	0.059	0.119	0.092
487.500	0.057	0.116	0.090
488.302	0.057	0.116	0.089
489.779	0.056	0.115	0.088
492.000	0.056	0.114	0.087
492.825	0.055	0.113	0.087
496.600	0.054	0.111	0.085
497.390	0.054	0.111	0.084
501.187	0.052	0.109	0.083
501.200	0.052	0.109	0.083
501.997	0.052	0.108	0.082
505.800	0.051	0.106	0.080
506.646	0.051	0.106	0.080
510.500	0.049	0.104	0.078
511.339	0.049	0.103	0.078
512.861	0.049	0.102	0.077
515.200	0.048	0.101	0.076
516.075	0.048	0.101	0.076
520.000	0.047	0.099	0.074
520.855	0.046	0.098	0.074
524.800	0.045	0.096	0.072
524.807	0.045	0.096	0.072
525.679	0.045	0.096	0.072
529.700	0.044	0.094	0.070
530.548	0.044	0.094	0.070
534.600	0.043	0.092	0.068

Continuation of Table D.1			
$\lambda[\mu\text{m}]$	$F_{\nu}(\text{DL2014})$	$F_{\nu}(\text{PL+OTMBB})$	$F_{\nu}(\text{PL+GMBB})$
535.462	0.042	0.092	0.068
537.032	0.042	0.091	0.067
539.500	0.041	0.090	0.066
540.422	0.041	0.089	0.066
544.500	0.040	0.088	0.064
545.427	0.040	0.087	0.064
549.500	0.039	0.086	0.063
549.541	0.039	0.086	0.063
550.479	0.039	0.085	0.062
554.600	0.038	0.084	0.061
555.578	0.038	0.083	0.061
559.800	0.037	0.082	0.059
560.723	0.036	0.081	0.059
562.341	0.036	0.081	0.059
564.900	0.036	0.080	0.058
565.917	0.035	0.079	0.057
570.200	0.035	0.078	0.056
571.159	0.034	0.078	0.056
575.400	0.034	0.076	0.055
575.440	0.034	0.076	0.055
576.449	0.033	0.076	0.054
580.800	0.033	0.074	0.053
581.788	0.032	0.074	0.053
586.100	0.032	0.073	0.052
587.177	0.031	0.072	0.051
588.844	0.031	0.072	0.051
591.600	0.031	0.071	0.050
592.615	0.031	0.071	0.050
597.000	0.030	0.069	0.049
598.104	0.030	0.069	0.049
602.560	0.029	0.068	0.048
602.600	0.029	0.068	0.048
603.644	0.029	0.067	0.047
608.100	0.028	0.066	0.046
609.235	0.028	0.066	0.046
613.800	0.027	0.064	0.045
614.878	0.027	0.064	0.045
616.595	0.027	0.064	0.044
619.400	0.027	0.063	0.044
620.573	0.026	0.063	0.044
625.200	0.026	0.061	0.043
626.321	0.026	0.061	0.042
630.957	0.025	0.060	0.041
631.000	0.025	0.060	0.041
632.122	0.025	0.060	0.041
636.800	0.024	0.059	0.040
637.977	0.024	0.058	0.040
642.700	0.024	0.057	0.039
643.886	0.024	0.057	0.039
645.654	0.023	0.056	0.039
648.600	0.023	0.056	0.038
649.850	0.023	0.056	0.038
654.600	0.022	0.054	0.037
655.869	0.022	0.054	0.037
660.693	0.022	0.053	0.036
660.700	0.022	0.053	0.036
661.943	0.022	0.053	0.036
666.800	0.021	0.052	0.035
668.074	0.021	0.052	0.035
673.000	0.020	0.051	0.034
674.262	0.020	0.050	0.034
676.083	0.020	0.050	0.034

Continuation of Table D.1			
$\lambda[\mu\text{m}]$	$F_{\nu}(\text{DL2014})$	$F_{\nu}(\text{PL+OTMBB})$	$F_{\nu}(\text{PL+GMBB})$
679.200	0.020	0.050	0.033
680.507	0.020	0.049	0.033
685.500	0.019	0.048	0.032
686.810	0.019	0.048	0.032
691.800	0.019	0.047	0.031
691.831	0.019	0.047	0.031
693.172	0.019	0.047	0.031
698.200	0.018	0.046	0.031
699.592	0.018	0.046	0.030
704.700	0.018	0.045	0.030
706.072	0.018	0.045	0.030
707.946	0.018	0.044	0.029
711.200	0.017	0.044	0.029
712.612	0.017	0.044	0.029
717.800	0.017	0.043	0.028
719.212	0.017	0.043	0.028
724.400	0.016	0.042	0.027
724.436	0.016	0.042	0.027
725.873	0.016	0.042	0.027
731.100	0.016	0.041	0.027
732.597	0.016	0.041	0.026
737.900	0.015	0.040	0.026
739.382	0.015	0.040	0.026
741.310	0.015	0.039	0.026
744.700	0.015	0.039	0.025
746.230	0.015	0.039	0.025
751.600	0.015	0.038	0.024
753.142	0.014	0.038	0.024
758.578	0.014	0.037	0.024
758.600	0.014	0.037	0.024
760.118	0.014	0.037	0.024
765.600	0.014	0.036	0.023
767.158	0.014	0.036	0.023
772.700	0.013	0.035	0.023
774.264	0.013	0.035	0.022
776.247	0.013	0.035	0.022
779.800	0.013	0.035	0.022
781.435	0.013	0.034	0.022
787.000	0.013	0.034	0.021
788.673	0.013	0.034	0.021
794.300	0.012	0.033	0.021
794.328	0.012	0.033	0.021
795.978	0.012	0.033	0.021
801.700	0.012	0.032	0.020
803.350	0.012	0.032	0.020
809.100	0.012	0.031	0.020
810.791	0.012	0.031	0.020
812.831	0.012	0.031	0.019
816.600	0.011	0.031	0.019
818.301	0.011	0.031	0.019
824.100	0.011	0.030	0.019
825.880	0.011	0.030	0.018
831.764	0.011	0.029	0.018
831.800	0.011	0.029	0.018
833.529	0.011	0.029	0.018
839.500	0.010	0.029	0.018
841.250	0.010	0.028	0.018
847.200	0.010	0.028	0.017
849.042	0.010	0.028	0.017
851.138	0.010	0.028	0.017
855.100	0.010	0.027	0.017
856.906	0.010	0.027	0.017

Continuation of Table D.1			
$\lambda[\mu\text{m}]$	$F_{\nu}(\text{DL2014})$	$F_{\nu}(\text{PL+OTMBB})$	$F_{\nu}(\text{PL+GMBB})$
863.000	0.010	0.027	0.016
864.842	0.010	0.026	0.016
870.964	0.009	0.026	0.016
871.000	0.009	0.026	0.016
872.853	0.009	0.026	0.016
879.000	0.009	0.025	0.015
880.937	0.009	0.025	0.015
887.200	0.009	0.025	0.015
889.097	0.009	0.025	0.015
891.251	0.009	0.024	0.015
895.400	0.009	0.024	0.015
897.332	0.009	0.024	0.015
903.600	0.008	0.024	0.014
905.643	0.008	0.023	0.014
912.000	0.008	0.023	0.014
912.011	0.008	0.023	0.014
914.031	0.008	0.023	0.014
920.400	0.008	0.023	0.013
922.497	0.008	0.022	0.013
929.000	0.008	0.022	0.013
931.041	0.008	0.022	0.013
933.254	0.008	0.022	0.013
937.600	0.008	0.021	0.013
939.665	0.008	0.021	0.013
946.200	0.007	0.021	0.012
948.368	0.007	0.021	0.012
954.993	0.007	0.020	0.012
955.000	0.007	0.020	0.012
957.152	0.007	0.020	0.012
963.800	0.007	0.020	0.012
966.017	0.007	0.020	0.012
972.700	0.007	0.020	0.012
974.965	0.007	0.019	0.011
977.237	0.007	0.019	0.011
981.700	0.007	0.019	0.011
983.995	0.007	0.019	0.011
990.800	0.007	0.019	0.011
993.109	0.007	0.019	0.011
End of Table			

Appendix E: Physical parameters for each galaxy of the studied sample

id	z	β_{FUV}	$\beta_{FUV, \text{err}}$	sSFR	sSFR_err	M_{dust}	$M_{\text{dust, err}}$	A_{FUV}	$A_{\text{FUV, err}}$	IRX	IRX_err	age_main	L_dust	L_FUV	SFR	M_{star}	$M_{\text{star, err}}$						
CANDELS_GOODSS_12	4.411	-2.144	0.146	1.115E+10	3.433E+10	0.014	0.004	1.589	0.095	0.658	0.051	205.268	68.803	3.444E+10	3.489E+10	47.427E21	1.189E+11	1.189E+11					
CANDELS_GOODSS_14	4.411	-1.465	0.066	1.226E+10	1.152E+10	1.158E+10	8.389E+10	1.920E+10	0.389	0.076	-0.218	0.109	1028.233	20.616	1.038E+10	1.725E+10	797.266E20	1.664E+10	8.318E+10	27.268	1.562	2.056E+10	1.354E+10
CANDELS_GOODSS_19	4.500	-0.558	0.109	2.079E+10	4.082E+10	0.004	7.390E+10	2.510	0.138	1.127	0.058	792.206	126.165	5.492E+10	6.808E+10	4.074E+10	2.037E+10	48.600	6.609	2.337E+10	3.318E+10		
CANDELS_GOODSS_21	4.572	-1.385	0.224	2.955E+10	1.182E+10	0.005	0.002	1.761	0.112	0.762	0.057	606.651	194.588	2.019E+10	1.697E+10	3.370E+10	3.186E+10	21.673	1.099	7.334E+10	2.878E+10		
CANDELS_GOODSS_32	4.411	-0.879	0.102	1.019E+10	1.902E+10	0.015	0.003	2.484	0.090	1.090	0.040	222.199	48.486	6.525E+10	5.007E+10	1.089E+10	8.551E+10	2.647E+10	72.815	6.798	7.149E+10	1.156E+10	

Table E.1: Physical parameters. Only the first rows are shown. For each object in the sample, the table contains the following information for PL+OT_MBB: id, redshift, β_{FUV} , sSFR, sM_dust, M_dust, A_FUV, IRX, age_main, L_dust, L_FUV, SFR, and M_star.

id	redshift	β_{FUV}	$\beta_{FUV, \text{err}}$	sSFR	sSFR_err	ΔM_{dust}	$\Delta M_{\text{dust, err}}$	A_{FUV}	$A_{\text{FUV, err}}$	IRX	IRX_err	age_main	L_dust	L_FUV	SFR	M_{star}	$M_{\text{star, err}}$						
CANDELS_GOODSS_12	4.411	-2.144	0.146	1.115E+10	3.433E+10	0.014	0.004	1.589	0.095	0.658	0.051	205.268	68.803	3.444E+10	3.489E+10	47.427E21	1.189E+11	1.189E+11					
CANDELS_GOODSS_14	4.553	-1.063	0.066	1.226E+10	1.152E+10	1.158E+10	8.389E+10	1.920E+10	0.389	0.076	-0.218	0.109	1028.233	20.616	1.038E+10	1.725E+10	797.266E20	1.664E+10	8.318E+10	27.268	1.562	2.056E+10	1.354E+10
CANDELS_GOODSS_19	4.500	-0.558	0.109	2.079E+10	4.082E+10	0.004	7.390E+10	2.510	0.138	1.127	0.058	792.206	126.165	5.492E+10	6.808E+10	4.074E+10	2.037E+10	48.600	6.609	2.337E+10	3.318E+10		
CANDELS_GOODSS_21	4.572	-1.385	0.224	2.955E+10	1.182E+10	0.005	0.002	1.761	0.112	0.762	0.057	606.651	194.588	2.019E+10	1.697E+10	3.370E+10	3.186E+10	21.673	1.099	7.334E+10	2.878E+10		
CANDELS_GOODSS_32	4.411	-0.879	0.102	1.019E+10	1.902E+10	0.015	0.003	2.484	0.090	1.090	0.040	222.199	48.486	6.525E+10	5.007E+10	1.089E+10	8.551E+10	2.647E+10	72.815	6.798	7.149E+10	1.156E+10	

Table E.2: Physical parameters. Only the first rows are shown. For each object in the sample, the table contains the following information for PL+OT_MBB: id, redshift, β_{FUV} , sSFR, sM_dust, M_dust, A_FUV, IRX, age_main, L_dust, L_FUV, SFR, and M_star.